The Vertical and Horizontal Performance of Pressed-In Sheet Piles

Timo Zheng

Supervised by Stuart Haigh

2019 - 2020

I hereby declare that, except where specifically indicated, the work submitted herein is my own original work.

Signed:

Date: 27^{th} May 2020

Technical Abstract

Sheet piles have long been used for temporary construction and simple earth retaining structures, with their use being predominantly limited to these applications at present. They are seen as less robust than other foundation solutions as a result of their low bending stiffnesses and small toe areas, meaning they are rarely considered for more complex designs. This has lead to a lack of knowledge surrounding their behaviour, particularly in terms of their vertical performance, which in turn feeds back into the hesitancy to use them. There are no widely accepted models or design methods specific to their use.

The press-in method is a relatively new way of installing piles, involving a static jacking force. It has considerable advantages over other methods such as driving or using vibration, especially in terms of the environmental disturbance it produces - noise and vibration during installation is minimal. Again, as the technology is less established than its alternatives, there is a void of existing research to support its widespread use. It is well known that a pile's performance is heavily dependent on how it is installed, meaning a clear understanding of the method's effects will be necessary for robust design of pressed-in piles.

This project therefore aims to stimulate much needed research in both of these areas to allow pressed-in sheet piles to be used with more confidence, leading to their wider deployment. It will attempt to provide a theoretical basis for analysing the vertical and horizontal performances of pressed-in sheet piles and suggest a possible route towards establishing a design method in future.

Three single piles and one group of three were installed under varying installation conditions and subjected to vertical and horizontal load tests using hydraulic jacks. The tests were performed in a novel liquefiable sand tank. By liquefying the sand between each pile installation, the effective stress of the soil can be reduced to zero, normally consolidating the soil and 're-setting' its stress history. This allows tests to be directly compared. Data was harvested using various sensors, including load cells, earth pressure sensors, and inclinometers.

Theoretical models based on vertical arching and plugging are presented to estimate the ultimate vertical capacity. The capacity was also found to vary significantly with the installation regime, with higher levels of surging causing larger reductions in capacity. The models are able to explain the data and fit all observed trends, though much more data would

be needed to increase confidence in them and refine their intricacies. A method for assessing the capacity retroactively from the installation loads easily and accurately is also identified.

The installation was found to be much less influential on the lateral performance of a sheet pile than the axial. Contrarily, surging was found to slightly stiffen the response as oppose to degrading it, meaning the effect of installation can be conservatively ignored. A simple modification to the P-y method is suggested for estimating the horizontal performance, to account for existing methods being suited to circular rather than flat cross sections. Additionally, within expected deformation limits, the behaviour was found to be approximately linear. On this basis, dimensionless design charts have been developed for lateral loading.

While all findings are harboured by the size and diversity of the obtained data set, the models and methods described are intuitive and make sense in accordance with existing literature; they are able to explain all the observations from testing, and have significant implications for design.

Notation

General Soil Properties

e	Voids ratio
e_{max}	Maximum voids ratio
e_{min}	Minimum voids ratio
I_D	Relative density
G_s	Specific gravity
K	Lateral earth pressure coefficient
K_p	Passive earth pressure coefficient
γ'	Effective unit weight
γ_w	Unit weight of water
W'	Effective weight of soil mass
ϕ'	Friction angle
ϕ'_{cs}	Critical state friction angle
ϕ'_p	Peak friction angle
σ'	Effective stress
σ'_h	Horizontal effective stress
σ'_v	Vertical effective stress
σ'_{v0}	In-situ vertical effective stress
p'	Mean effective stress
τ	Shear Stress
z	Depth below ground level
u_c	CPT pore water pressure
q_c	CPT cone resistance
k	Soil permeability
E_0	Young's modulus of soil
C_v	Coefficient of consolidation
T_v	Dimensionless time of consolidation
R_v	Degree of consolidation

Pile Properties

A_s	Cross sectional area
A_g	Gross cross sectional area
I	Second Moment of Area
L	Pile length below ground
D	Diameter of tubular pile
D_{eq}	Equivalent diameter of sheet pile
W	Width of sheet pile
E	Young's Modulus of steel
σ_y	Yield stress

Vertical Performance

N_q	Bearing capacity Factor
s_c	Shape factor for bearing
q_{bf}	Bearing pressure at failure
δ	Pile-soil interface friction angle
l_p	Plug-pile interface perimeter
l_s	Plug-external soil int. perimeter
τ_p	Plug-pile shear stress
τ_s	Plug-external soil shear stress
χ_{mob}	Friction mobilisation factor
F_{surge}	Surging reduction factor
V	Vertical head force
V_y	Vertical yield load
V_{max}	Vertical ultimate capacity

Horizontal Performance

e_F	Height of loading above ground
H	Horizontal head force
H_{max}	Horizontal ultimate capacity
k_{py}	Subgrade reaction modulus
P	Lateral soil force
P_u	Maximum lateral soil force
y	Lateral deflection
y_s	Lateral deflection at ground surface
F_k	Stiffness modification factor
F_p	Maximum pressure mod. factor
K_i	Ground surface pile stiffness
m_i	Max. moment p.u. deflection
R_s	Soil-pile stiffness ratio
M	Pile beding moment
S	Pile Shear
θ	Pile rotation
$\bar{m}$	Dimensionless m_i
$\bar{K}$	Dimensionless K_i

Table of Contents

1 Introduction

1.1 Pressed-In Sheet Piles

Sheet piles are structures set in the ground made of thin steel sheeting bent into a ‘U’ shape, as depicted in figure 1-1. They are easy to install, re-usable, lightweight, and interlocking geometries at the section ends allow the construction of continuous walls. These key advantages have led to their widespread adoption in certain applications. They are predominately used as earth retaining structures, such as retaining walls, and the vast majority of their use is in temporary construction, where stable excavations can be established quickly, and their re-usability brings cost and material savings.

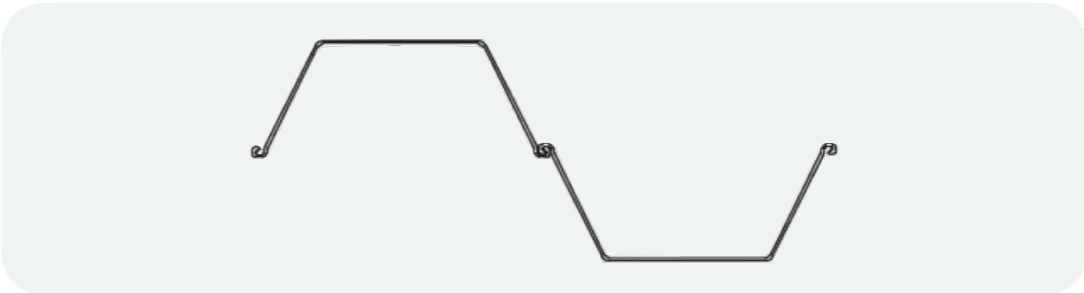

Figure 1-1: Typical cross section of a steel sheet pile (Steel Piling Group, 2020)

Traditionally, installation involves driving (applying large hammer blows to the pile head) or vibration, both of which cause high levels of disturbance (noise and vibration) to the surrounding environment. Giken are pioneers of the press-in technology - a method of installation involving the use of a static jacking force to push the pile into the ground (a.k.a. jacking). The reaction force required to keep the piling equipment grounded can be provided by a ballast, or rather conveniently by the rig anchoring itself to previously installed piles. Figure 1-2 demonstrates this principle. This method is incredibly efficient for installing lines of piles, and causes minimal disturbance - two considerable advantages over traditional methods. It’s drawback is that it is unable to install piles to as great depths as other methods, due to its more limited jacking force.

1.2 Motivation and Scope

The motivation for this project comes from an ambition to promote wider use of this innovative technology, and to stimulate much needed research in aid of the establishment of a literature which is currently sparse. In fact, the latter is a prerequisite for the former.

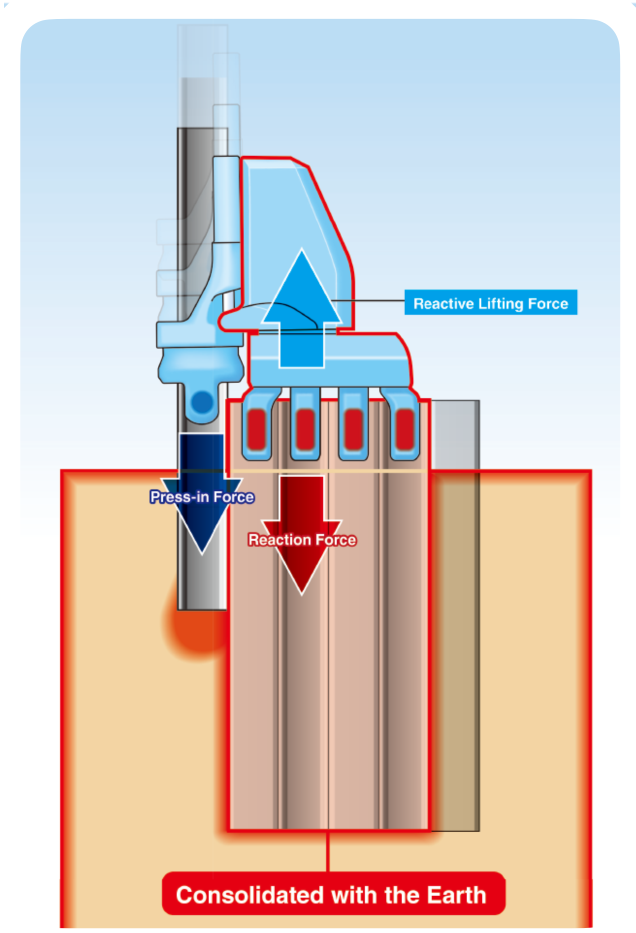

Figure 1-2: Reaction mechanism for a Giken 'Silent Piler' (Giken, 2020)

As mentioned in section 1.1, sheet piles are currently limited in their uses, and are rarely seen in the context of permanent construction. Being typically more flexible and significantly less substantial than other foundation solutions, they appear to be less robust, and are therefore rejected in much other than simple cases, leading to a lack of knowledge in their fundamental behaviour. Better understanding in this respect will lead to greater confidence in predictions and assessments of their performance. Along with the advantages of the press-in method (which are not limited to temporary works and basic construction), this may lead to their adoption in more novel problems. Basement enclosures, coastal structures, and even building foundations are examples Giken has cited.

The press-in method, being newer and less widely used than traditional installation methods, also suffers from a void of relevant literature. It is well known that the processes that occur during installation of a pile have a significant effect on its resulting performance. As such, since the press-in method is inherently different to other techniques, the effect on the surrounding soil and pile performance will undoubtedly be changed.

This project aims to investigate the response of sheet piles to vertical and horizontal loads, with particular focus on how they are affected by the press-in process. It will attempt to apply existing soil mechanics principles as well as create new models where necessary to better understand these issues. While of course limited in its scope, it looks to provide some of the fundamental theory and concepts which may lead towards the development of a formalised design method in the future. This would potentially be a catalyst for increased usage of the technology, bringing many benefits to the construction sector across the world.

2 Literature Review

Typically there are four aspects of pile design. These are the strengths and stiffnesses in the the axial and lateral directions, which tend to be considered independently.

2.1 Vertical Capacity in Sand

For vertical capacity, current design methods vary greatly for different installation types. For displacement piles, which include sheet piles, methods tend to be highly empirical, due to complex stress histories in the soil being induced during installation. Capacity evaluation generally comprises estimating the base resistance at the bottom of a pile and the shaft friction along its length - design methods attempt to provide these stresses based on soil properties.

The shaft resistance is particularly affected by installation, and as such, all standard methods are empirical. The API method (2000) is a widely accepted approach which details K and δ for a given soil type such that the shear stress at the pile can be calculated as $\sigma_{v0} \cdot K \tan \delta$, which varies along the pile length. It is based on a database of un-instrumented pile tests and is purely a fit to the data.

The base resistance is governed by the bearing capacity of sand, which alternatively, can be described analytically. The strength of sand is provided by its confining stress, and in bearing there are two origins of this - the surcharge acting at the level of the bearing plane (including self weight of the above soil), and the self weight of soil within the slip mechanism. The latter becomes negligible at depth as the ratio of mechanism height to overbearing soil height reduces dramatically, so it is ignored:

$$q_{bf} = s_c N_q \sigma'_{v0} \text{ with } N_q = \tan^2\left(\frac{\pi}{4} + \frac{\phi'}{2}\right) e^{\pi \tan \phi'} \tag{2.1}$$

This solution for N_q (Prandtl, 1920) is analytical and exact. The shape factor s_c is instead found numerically. While exact closed-form solutions are not available as a function of the geometry of the foundation footprint, several curve fits to numerically produced results exist. This thesis will adopt that used by Eurocode 7 for a rectangular section:

$$s_c = 1 + \frac{B}{L} \sin \phi' \tag{2.2}$$

The API method also specifies empirically derived values of N_q for different soil types, though the analytical approach described is favoured as more accurate.

Sands denser than critical state will dilate on shearing, and hence have a peak friction angle ϕ'_p greater than their critical state value. Bolton (1986) produced a set of correlations quantifying the variation of ϕ'_p with relative density and confining stress. For a quartz sand:

$$I_R = I_D I_C - 1 = \frac{e - e_{min}}{e_{max} - e_{min}} \cdot \ln\left(\frac{20000\ \text{kPa}}{p'}\right) - 1 \tag{2.3}$$

Relative dilatancy I_R can be related to the peak friction angle; in axisymmetric conditions:

$$\phi'_p = \phi'_{cs} + 3I_R \tag{2.4}$$

Equation 2.1 refers to ϕ'_p, but this is itself dependent on q_{bf} through confining stress. Starting with $\phi' = \phi'_{cs}$ to evaluate an initial q_{bf}, a representative mean stress within the failure mechanism can be taken as $p' = \sqrt{q_{bf} \cdot \sigma'_{v0}}$. This allows for the calculation of a new $\phi' = \phi'_p$; this procedure can then be iterated until the true solution is found.

2.2 Surging and Friction Fatigue

Key to the press-in methodology is the process of surging, where the pile is cyclically pressed in and pulled out during installation. The length of the insertion and removal strokes can be varied (with the insertion always being greater). It causes a reduction of the required penetration force, allowing piles to be installed to greater depths.

Friction fatigue is a phenomenon whereby cyclic loading of soil at a pile-soil interface causes a reduction in skin friction. Repeated shearing densifies the near-field soil and leads to a relaxing of horizontal pressure and hence friction (White and Bolton, 2002). Cyclic shearing is of course encountered during the installation of displacement piles, for both driving and jacking. However, the characteristics of the cycles themselves are different for these two methods; driving consists of only downwards strokes, with only slight upwards pile movement due to elastic rebound, whereas jacking employs explicit upwards strokes. It has been shown that one-way cyclic loading, as neighbouring soil experiences during driving, will induce less horizontal stress reduction than two way cycling, as observed during surging (White and Lehane, 2004). The need for a separate design method unique to jacked piles stems naturally from this. Since the API method and other similar procedures are predominantly based on empirical evidence from driven pile testing, they may not apply so well to jacked piles.

Some work has been done on the influence of surging (Burali d'Arrezo, 2015), though the relationship between it and friction fatigue remains complex. While surging is demonstrated to generally reduce pile capacity as a result of friction fatigue, there is not a simple correlation. For example, Burali d'Arrezo argues that there comes a point where reducing the surge stroke length further (i.e. increasing the amount of cycling) will actually increase the horizontal pressure.

2.3 Sand Plugging and Vertical Arching

For an open-ended tubular pile, penetration into the ground can occur via two mechanisms - (a) the pile progresses while the internal soil column (the plug) remains in place, known as unplugged penetration, or (b) the plug moves with the pile, known as plugged penetration (see figure 2-1). The mechanism which provides least resistance will take place, meaning both must be considered.

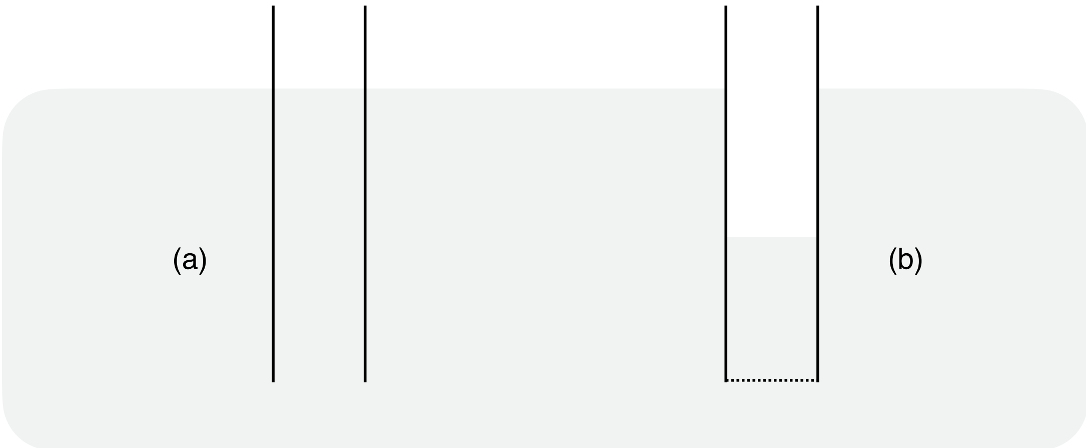

Figure 2-1: Unplugged (a) and plugged (b) modes of penetration

Kishida and Isemoto (1977) found that in sand, the internal soil column experiences a high degree of compaction, and thus produces high internal skin friction. This phenomenon is vital in determining the unplugged capacity. The stress distribution within an inner soil column of diameter D and interface friction angle δ can be found by modelling a small soil element within the soil plug of height δz (Randolph, 1991), as in figure 2-2. For a fully rough pile ($\delta = \phi'$), integrating the equilibrium of forces leads to:

$$\sigma_v' = \frac{D\gamma'}{4K\tan\phi'} \cdot \left(e^{\frac{4K\tan\phi'}{D}z} - 1\right) \tag{2.5}$$

The exponential variation of stress with depth is a result of feedback loop, whereby increasing vertical stress causes skin friction to rise, which in turn drives up the vertical stress. This is

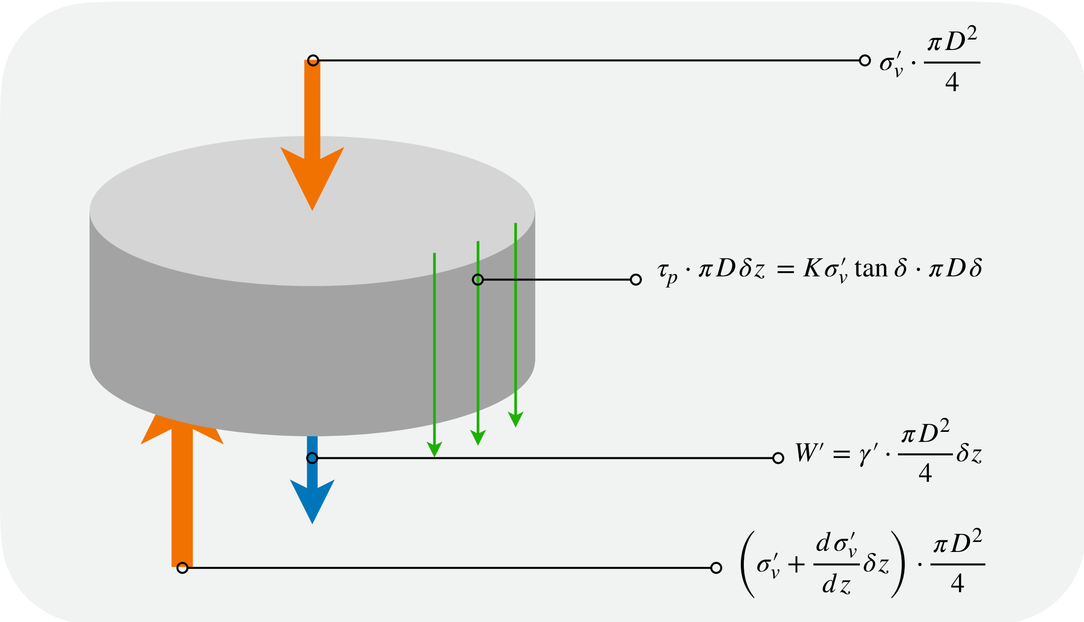

Figure 2-2: Forces acting on a small element of the inner soil column during loading

known as vertical arching. The value of K during penetration can be calculated by analysing the resulting Mohr's circle (figure 2-3) for soil at the interface, where there must be failure on the plane of the interface to allow for the relative sliding. This leads to:

$$K = \frac{1 - \sin^2 \phi'}{1 + \sin^2 \phi'} \tag{2.6}$$

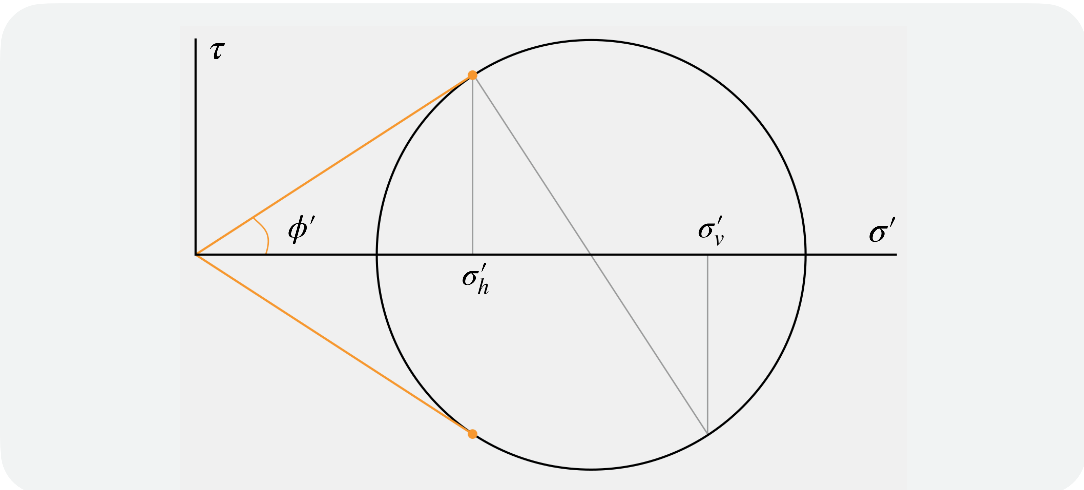

Figure 2-3: Mohr's circle at pile-soil interface

This appears to be similar to the expression for $K_a = 1/K_p$ (see section 2.5), though differs in that the horizontal stress is not principal here. For K_a, σ'_h is at the very left of the Mohr's circle as there is no shear on its plane, whereas here, it is closer to the centre since the shear must be fully mobilised (due to sliding).

While plugging and arching have primarily been explored for tubular piles, plugging has been observed in sections without bounded inner soil columns, such as H-piles (Alves et al., 2020), meaning similar ideas could be applied.

2.4 Vertical Stiffness in Sand

The vertical stiffness of a pile in sand is typically evaluated by treating the ground as an elastic material with shear stiffness. As will be seen, this aspect is not particularly relevant to the content of this project, so will not be considered here.

2.5 Horizontal Capacity in Sand

The horizontal capacity of a pile can be derived by considering its loading at failure. This stems from earth pressure theory which states that there is a maximum horizontal pressure $\sigma'_{h,max}$ that soil can sustain. As in figure 2-4, by considering a pivot point at some depth and setting the pressures as maximum at all depths, horizontal and moment equilibrium equations will yield the depth of pivot and load at failure.

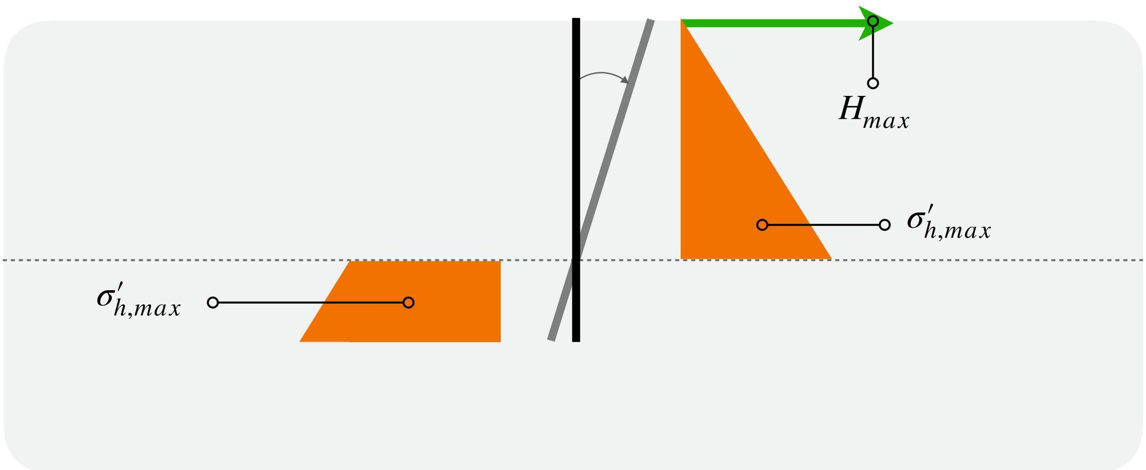

Figure 2-4: Loading configuration at lateral failure

Rankine (1856) derived a lower bound solution for this maximum soil pressure using a planar failure surface, for the case of a plane strain smooth wall in sand:

$$\sigma'_{h,max} = K_p \sigma'_{v0} = \frac{1 + \sin \phi'}{1 - \sin \phi'} \cdot \sigma'_{v0} \tag{2.7}$$

In other words, if an infinitely long wall is moved laterally, the above limiting stresses will eventually be reached. A pile moving laterally will also encounter limiting horizontal stresses, though they will be larger due to end effects at the edge of the pile - the end planes provide additional resistance. Additionally if there is interface friction, there will be further increases. An empirical approach using model tests suggests that for piles, sand is able to provide a pressure of $K_p^2\sigma'_{v0} = \left[(1+\sin\phi')/(1-\sin\phi')\right]^2 \cdot \sigma'_{v0}$ (Prasad and Chari, 1999). This result is generally accepted, however, once again it is obtained from tubular pile geometries, and may not apply to sheet piles, which are more similar to very short walls. There has been little research into the variation of K_p accounting for 3D effects. Soubra et al. (2000) have developed 3D upper bound mechanisms comprising sliding blocks, which show that K_p increases significantly. Supporting literature is thin however, and the paper lacks experimental validation, so the results of Prasad and Chari are currently considered the most applicable to sheet piles.

2.6 Horizontal Stiffness in Sand

The lateral deflection of deep foundations can be modelled using the P-y method. First described by Reese and Matlock (1956), it involves discretising the pile into small elements whose movement is constrained by non-linear horizontal springs (representing the soil), as well as beam bending (see figure 2-5 left). The response of each spring takes the form of a P-y curve. The first formulation for these was presented by Reese et al. (1974), and involves four sections - linear, hyperbolic, linear, and constant. This formulation was adapted into a similar, continuous hyperbolic form by O'Neill and Murchison (1983), to allow for smoother computational manipulation. This curve is shown in figure 2-5 right where the parameters P_u and k_{py} are determined by the empirically generated correlations in figure 2-6, and $A = \max(0.9, 3 - 0.8z/D)$.

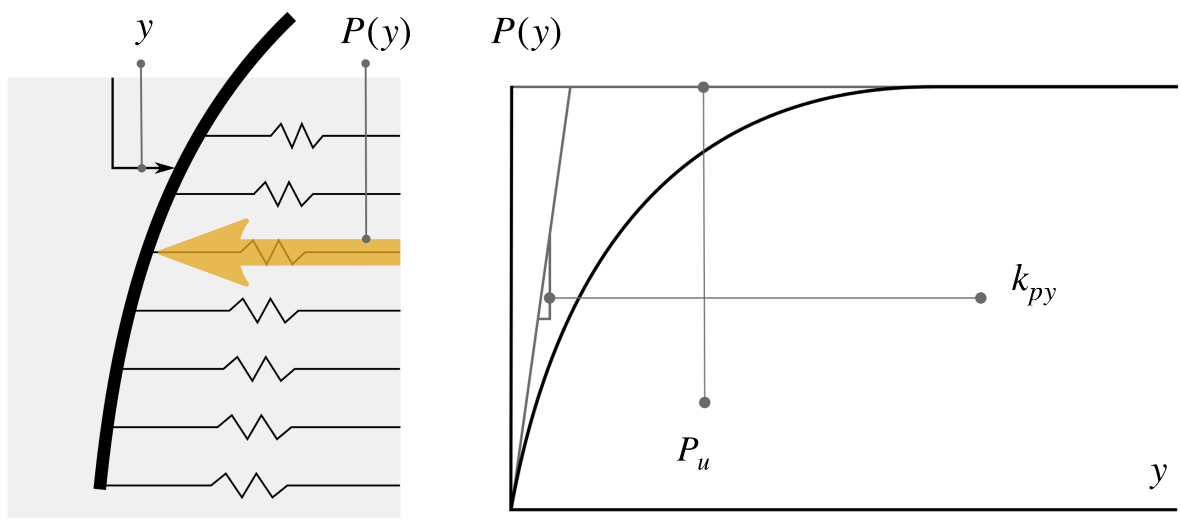

$$P = AP_u \tanh\left(\frac{k_{py}z}{AP_u}y\right)$$

Figure 2-5: The P-y formulation

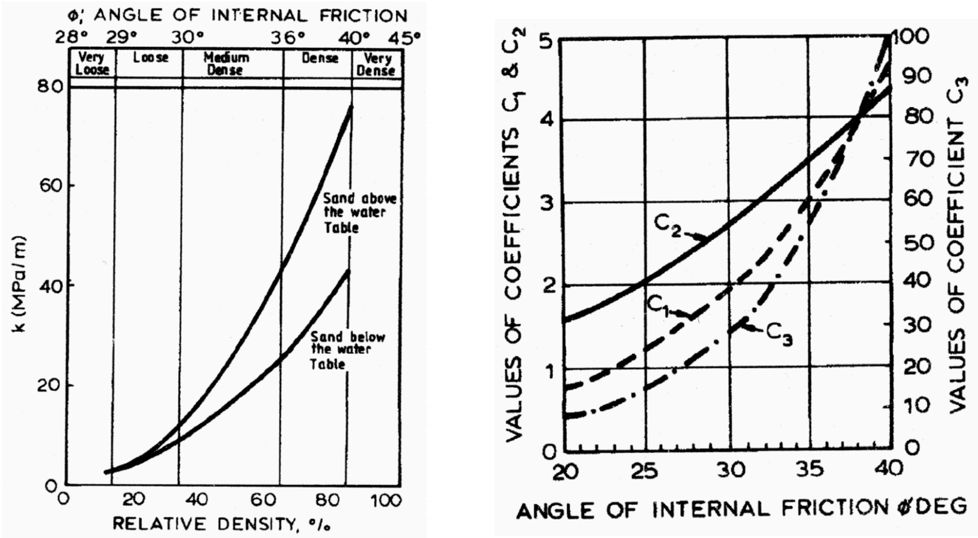

$$P_u = \min\ \left((C_1 z + C_2 D)\gamma' z\ , C_3 D \gamma' z\right)$$

Figure 2-6: Empirically derived p-y curve coefficients

The governing equation in the absence of vertical loading, which can be solved via a finite difference method, is:

$$EI \frac{d^2 y}{dz^2} + P(y) = 0 \tag{2.8}$$

This analysis should in theory apply to any shape of pile, since it takes into account the pile's properties. However, the empirical correlations used to define the soil response are derived using data from tubular piles only. Modification may therefore be needed to account for differences in how a sheet pile interacts with the soil compared to a circular section.

2.7 CPT Interpretation

Many of the methods described above rely on soil properties, hence site investigation is necessary. The relative density will prove particularly crucial in that it determines peak friction. An empirical correlation between I_D and the cone resistance from a CPT is given by Jamiolkowski et al. (2001):

$$I_D = 0.268 \ln\left(\frac{q_c / P_a}{\sqrt{\sigma'_{v0}/P_a}}\right) - 0.675 \tag{2.9}$$

where P_a is atmospheric pressure. There have been other correlations, such as from Schmertmann (1976) and Baldi et al. (1986). Jamiolkowski's is chosen as it is presented as an improvement on existing methods. That being said, the reliability of any estimates using CPT data is questioned, even by Jamiolkowski himself. It will be used here in absence of any other option, as even a crude estimate of the level of dilatancy/peak friction will be required.

3 Methodology

To investigate the vertical and horizontal behaviour of sheet piles and the effect of installation method, multiple full-scale load tests were carried out on an instrumented pile for different installation regimes in a large tank of sand. These tests were carried out during summer 2019 in partnership with Giken at their headquarters in Kochi, Japan.

3.1 Test Field

All testing took place in a 7 x 7 x 10 m deep facility filled with silica sand. The key feature of the tank is its ability to be liquified (figure 3-1). Water is pumped into the tank at the bottom, and flows through the sand up to and over the top, where it is recirculated back into the pumps. The finite permeability of the sand (and weight of water) mean that the water must be pressurised in order to flow upwards. The water pressure will reduce linearly from the bottom to top of the tank with a gradient of $du/dz = \gamma_w(1 + v/k)$, where v and k are the water velocity and soil permeability. Since $d\sigma_v/dz = \gamma$, if the flow rate is such that the velocity reaches $v = k(\gamma/\gamma_w - 1)$, the effective stress within the soil the will be set to zero everywhere.

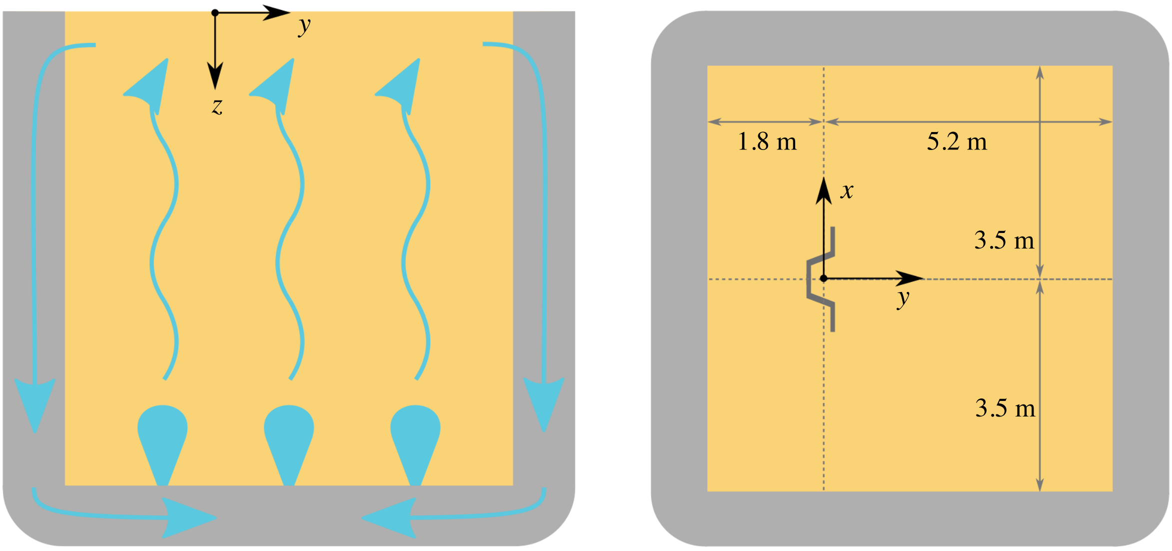

Figure 3-1: Soil tank geometry and liquefaction process

Following this, the sand is normally consolidated, and its stress history effectively 'reset'. By liquifying the tank after each test, all can be run with the same soil conditions.

3.2 Test Cases

3.2.1 General Procedure

The full test encompassed 4 cases, each subject to different conditions. Cases 1-3 involved a single pile, and case 4 a wall of three. For each, testing consisted of the following, separated by at least 24 hours:

Boiling The soil tank is liquified.

Installation The pile(s) was installed via jacking in the location indicated in figure 3-1. Also indicated is a sign convention which will be used from here onwards. During surging, the press-in speed was 65 mm/s, and the pull-out speed was 100 mm/s. For each case, surge stroke lengths were specified, as well as a maximum force criteria - if the penetration force reaches this value, the current stroke is terminated and the pull-out begins, resulting in smaller surge cycles.

Axial Test The pile(s) was subjected to an increasing vertical head load via a hydraulic jack until the ultimate load or a displacement of $D_{eq}/10$ (figure 3-2) was reached. The rate of loading, which varied between 5 and 70 mm/hr, was slow enough for pseudo-static behaviour to be assumed.

Lateral Test The pile(s) was subjected to an increasing horizontal head load in the y direction until the ultimate load or a displacement of $D_{eq}/30$ was reached. Again the rate of loading (~40 mm/hr) was sufficiently slow.

Extraction The pile(s) is extracted.

The deflection limits specified for the load test are informed by Japanese codes for pile testing (JGS 1810, 2010 and JGS 1811, 2002). D_{eq} is found by considering the pile as an equivalent tubular pile with equal steel area and enclosed area (figure 3-2).

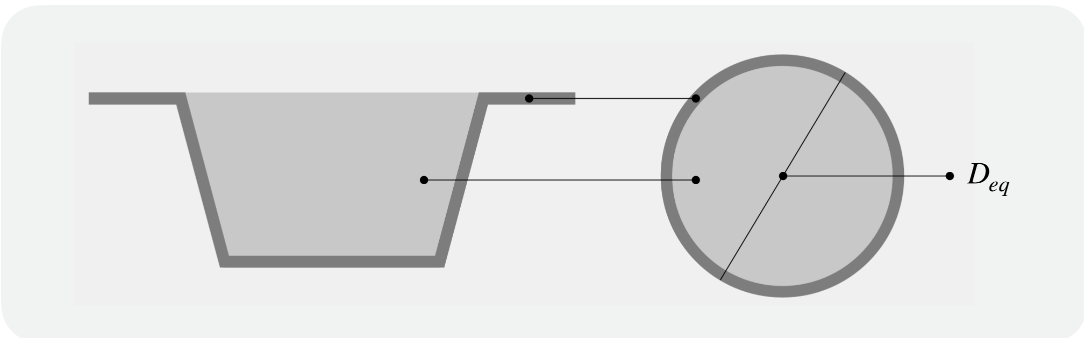

Figure 3-2: Equivalent tubular pile

3.2.2 Case Parameters

A summary of the differences between cases is presented in table 3-1.

Table 3-1: Differences between test cases

Case	No. of Piles	Water Table Depth	Surge Stroke Length (down/up)	Maximum Force (kN)	L (m)	e_F (m)
1	1	7 m	400/200 mm	800	6.15	1.19
2	1	1 m	400/200 mm	800	6.04	1.30
3	1	1 m	100/50 mm	300	6.19	1.15
4	3	1 m	100/50 mm	300 → 350	5.84	1.50

3.3 Equipment and Instrumentation

An 8.15 m long SP-25H steel sheet pile was used. The steel has a Young's Modulus of $E = 210$ GPa and a yield stress of $\sigma_y = 295$ MPa. The cross section, its dimensions and relevant properties are shown in figure 3-3. The adjacent piles demonstrate the arrangement of case 4.

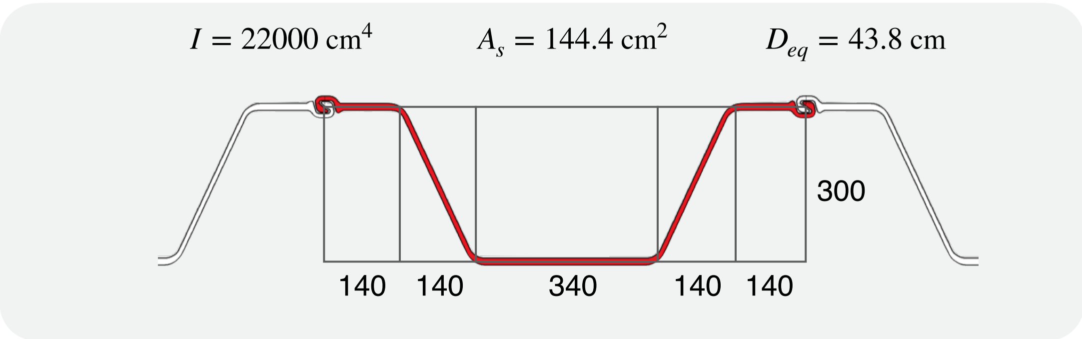

Figure 3-3: Pile geometry

A range of sensors were used to monitor pile and soil behaviour, shown in figure 3-4. Note that the strain gauges aimed to measure base force, but the data isn't considered in this report. Calibration proved difficult with gauges giving wildly different results to each-other, and as will be seen, base effects act on a soil plug, transferring to the pile via skin friction along the length, so gauges only at the bottom actually provide little insight. The pressure sensors measure horizontal pressure in the radial direction from the pile. Due to anomalous readings of in-situ stress after setting, the pressure differentials will be considered as oppose to absolutes. Additionally, the piler itself is able to measure the applied force and cumulative pile movement during installation over time.

3.4 Processing Methods

The analysis concerning vertical performance is predominantly based on the raw data obtained from the instrumentation, and any processing is fairly minimal and/or self-

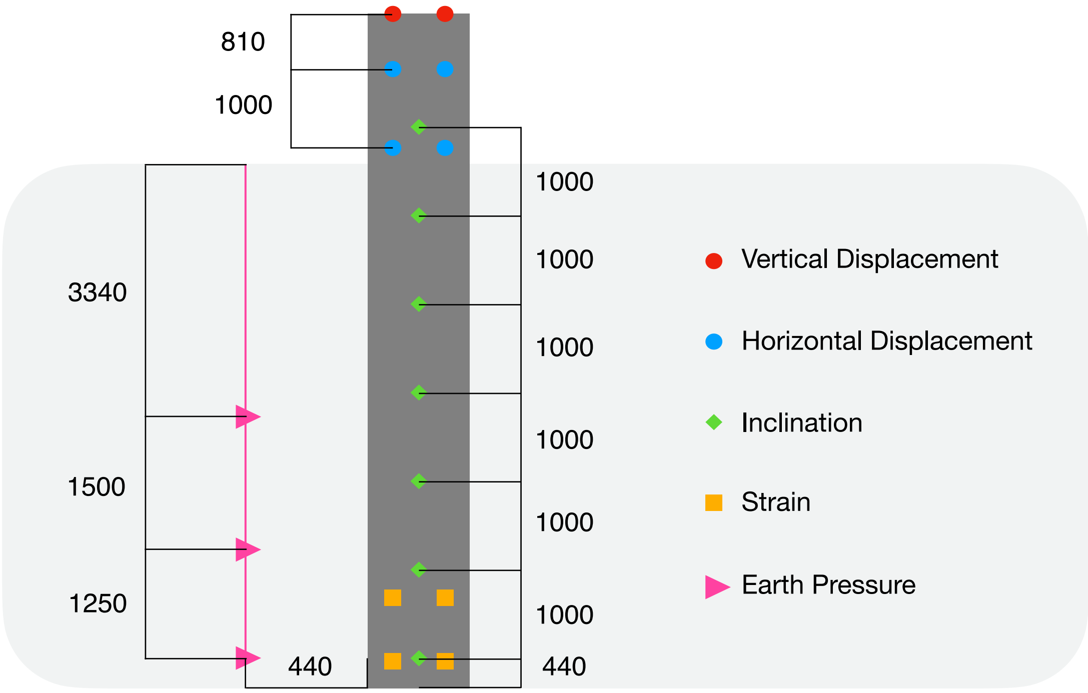

Figure 3-4: Sensor locations

explanatory. For the horizontal performance, two pieces of software were used in aid of the analysis, which will be explained here.

3.4.1 'Probfit'

The rotations along the length of the pile, along with the displacements at the top, can be numerically integrated to give the deflected shapes. Theoretically, they can be also be numerically differentiated to give the bending moment, shear and soil pressure via the following relationship:

$$P = \frac{\mathrm{d}S}{\mathrm{d}z} = \frac{\mathrm{d}^2 M}{\mathrm{d}z^2} = EI\,\frac{\mathrm{d}^3\theta}{\mathrm{d}z^3} = EI\,\frac{\mathrm{d}^4 y}{\mathrm{d}z^4} \tag{3.1}$$

However, where noise and error is attenuated during integration, it is amplified during differentiation. The raw data quickly becomes incoherent when differentiated. The 'Probfit' software, developed by Andrei Dobrisan, is designed to overcome this issue. The code is too complex to present in full, but it works on the following principles.

It takes as input rotation and deflection data points; boundary conditions on shear, moment and pressure at certain depths; the bending stiffness and error ranges for the above. It then generates a large number of n-degree polynomials (10^6 of order 8 when used here) as possible $y(z)$, and by differentiating them, creates families of curves corresponding to y, θ, M, S and P. Each family is compared to the inputs and associated error ranges, and by selecting only those for which all functions fit within all prescribed error bars, bounded regions of possible solutions are found for each y, θ, M, S and P.

The boundary conditions used for this project were $M = He_F$, $S = H$ and $P = 0$ at the surface, and $M = S = 0$ at the base. The error ranges were chosen with some sense of trial and error (until the output was deemed physically valid), but under the prevailing assumption that inclinometer and displacement error bars were approximately absolute in size. Once suitable values had been found for the highest load (3%, 4% and 5% of the highest recorded value for displacement, inclination and load respectively), they were factored up appropriately for use at lower loads, where inclinations and displacements are also smaller.

One final note is that a process of iteration was used to yield more precise results. The left two plots in figure 3-5 show the initial output for displacement and pressure from a particular test. Physically, the depths of zero deflection and pressure must coincide; we can see from the pressure curve that it appears to be below 4.8 m. Forcing deflection below 4.8 m to be negative via the input conditions provides a less uncertain output (figure 3-5 right).

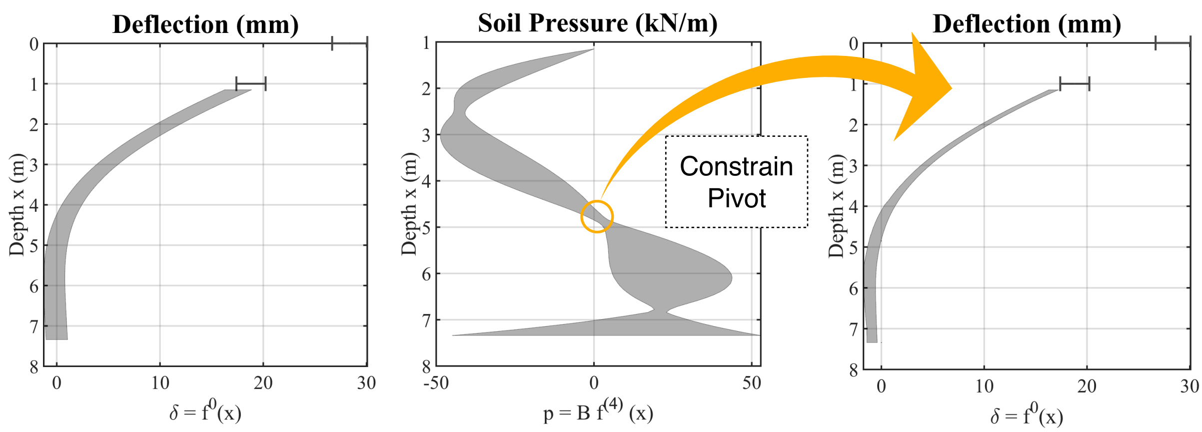

Figure 3-5: ‘Probfit’ iteration

3.4.2 P-y Simulation

As mentioned, the P-y method can be implemented via a finite difference discretisation. The full method is not presented here but can be found in Reese and Van Impe (2010).

The formulation has been implemented in python using an iterated linear algebra solver - the code is shown below. Given soil, pile and loading parameters, it outputs the deflections, bending moments and soil pressures along the pile’s length as well as surface displacement, maximum bending moment and maximum soil pressure. Surface displacement has been chosen over head displacement as it is what is specified by Japanese codes. Note that the P-y curves used are modified from section 2.7 by two factors F_k and F_p. These will be explained in section 6.

```
## Create matrix for finite difference solution
def solver(H,M,h,n,kpy,EI):
    mat=np.zeros((n,n))
    mat[0,0]=1                      ## Boundary Conditions at base
    mat[0,1]=-2
    mat[0,3]=2
    mat[0,4]=-1
    mat[1,1]=1
    mat[1,2]=-2
    mat[1,3]=1
    for i in range(2,n-2):          ## Finite difference equation
        mat[i,i-2] = 1
        mat[i,i-1] = -4
        mat[i,i] = 6+kpy[i]*h**4/EI ## kpy is a list of kpy at different z, outer two at each end of
        mat[i,i+1] = -4             ## pile correspond to imaginary nodes but aren't used
        mat[i,i+2] = 1
    mat[n-2,n-4]=1                  ## Boundary conditions at head
    mat[n-2,n-3]=-2
    mat[n-2,n-2]=1
    mat[n-1,n-5]=1
    mat[n-1,n-4]=-2
    mat[n-1,n-2]=2
    mat[n-1,n-1]=-1

    rhs=np.zeros((n,1))             ## Right hand side vector
    rhs[n-1,0]=2*h**3*H/EI
    rhs[n-2,0]=M*h**2/EI

    return(np.linalg.solve(mat,rhs))

## Create p-y curve
def py(z,D,gamma,ki,c1,c2,c3,y):
    A = max(0.9,3-0.8*z/D)
    pu=min((c1*z+c2*D)*gamma*z,c3*D*gamma*z)*F_p
    if z==0:
        return(0)
    else:
        return (A*pu*math.tanh(ki*F_k*z*y/(A*pu)))

def pile_sim(L,num_el,F,e,n,ki,EI,D,gamma,c1,c2,c3,F_k,F_p):
    ## Initial iteration
    h=L/num_el
    H=F
    M=F*e
    kpy=np.zeros(n)
    kpy.fill(ki)
    y0=solver(H,M,h,n,kpy,EI)

    ## Next iterations (iterate until y_head changes by ..%)
    z=np.zeros(n)
    p=np.zeros(n)
    for i in range(n):
        z[i]=(n-i-3)*h
        p[i]=py(z[i],D,gamma,ki,c1,c2,c3,y0[i])
        kpy[i]=p[i]/y0[i]
    y1=solver(H,M,h,n,kpy,EI)

    while(y1[n-3]/y0[n-3]>1.005):
        y0=y1
        for i in range(n):
            z[i]=(n-i-3)*h
            p[i]=py(z[i],D,gamma,ki,c1,c2,c3,y0[i])
            kpy[i]=p[i]/y0[i]
        y1=solver(H,M,h,n,kpy,EI)

    ## Calculate Bending Moment
    Moments=np.zeros(n)
    Moments[n-1]=F*(e-2*h)
    for i in range(1,n-1):
        Moments[i]=EI*(y1[i+1]-2*y1[i]+y1[i-1])/(h**2)

    ## Return values
    return [y1,Moments,p,y1[-3],np.amax(Moments),np.amax(p),z]
```

4 Site Conditions

4.1 Laboratory Testing

Giken performed laboratory testing on 6 soil samples from the site. Density testing and triaxial tests were carried out. From the density testing it was found that $G_s = 2.634$, $e_{min} = 0.531$ and $e_{max} = 0.891$. From the triaxial testing, unsaturated samples had a cohesion of 2.4 kPa and $\phi'_{cs} = 31.2°$. The saturated samples showed no cohesion and gave $\phi'_{cs} = 30.2°$. The cohesion of the unsaturated soil is negligible, and as such, the sand will be assumed purely frictional with a critical state friction angle as an average of the two tests, $\phi'_{cs} = 30.7°$.

4.2 In-Situ Testing

A Swedish Weight Sounding test was used to determine the repeatability of the liquefiable soil tank (i.e. how effectively the boiling of the tank returns the soil to initial conditions). Giken have provided results documenting equivalent SPT N-Values before and after liquefaction, shown in figure 4-1.

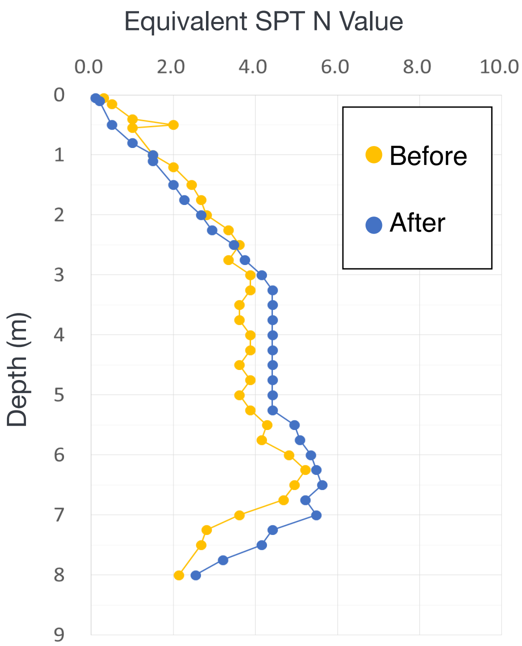

Figure 4-1: Effects of liquefaction process on soil resistance

The soil resistance profile derived from the second test agrees well with the first, albeit with some strengthening below 3 m depth. Within the region of concern for the tests (up to ~ 6m) the maximum discrepancy is around a 10% increase. While this is not entirely negligible, it is indeed small, and its effect through multiple test and boils is not possible to model. Analysis for all tests will therefore make use of the same soil profile.

Multiple Cone Penetration Tests were also carried out. 6 were performed before testing commenced for the low water table configuration (series 1), and 2 after completion (series 2), for the high water table.

A summary is given in figure 4-2, and the results for tip resistance and pore water pressure in figure 4-3. The data is used to construct soil profiles (for both the low and high water table cases), which will form the basis of the analysis in later sections.

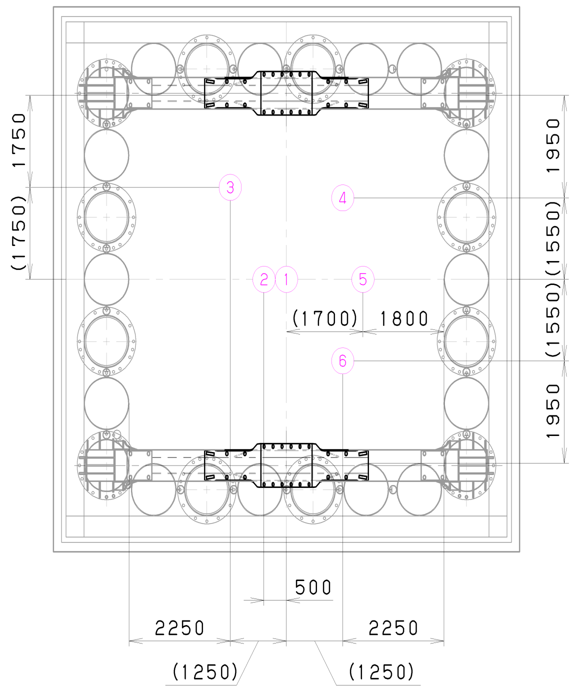

CPT	Series	Location No.
A	1	1
B	1	2
C	1	3
D	1	4
E	1	5
F	1	6
G	2	1
H	2	5

Outlined rows indicate CPT at location where piles were installed

Figure 4-2: CPT locations

Looking at the pore water pressures, there are low u_c values above the water table (which can be seen at ~ 7 m) for cases A-F. These are likely the result of partial saturation. They are small however, and the soil is presumed dry with the water table below all depths of interest. For cases G and H, there is noise close to the ground surface, but a clear hydrostatic pressure distribution is seen. The dashed line shows a linear fit to this, intercepting the zero pressure line at $z = 1$ m. This is in agreement with the design of the experiment which placed the water table at 1 m depth. For tests with the high water table, the sand is considered dry above 1 m, and saturated below.

From the tip resistances, it can be seen that there is some variation laterally across the site. To reduce complexity of the soil profile, only the CPTs performed at the location of the pile installations are considered, as they are most representative of what each pile 'sees'. This relies on the assumption that the region of soil mobilised is small compared to the distance

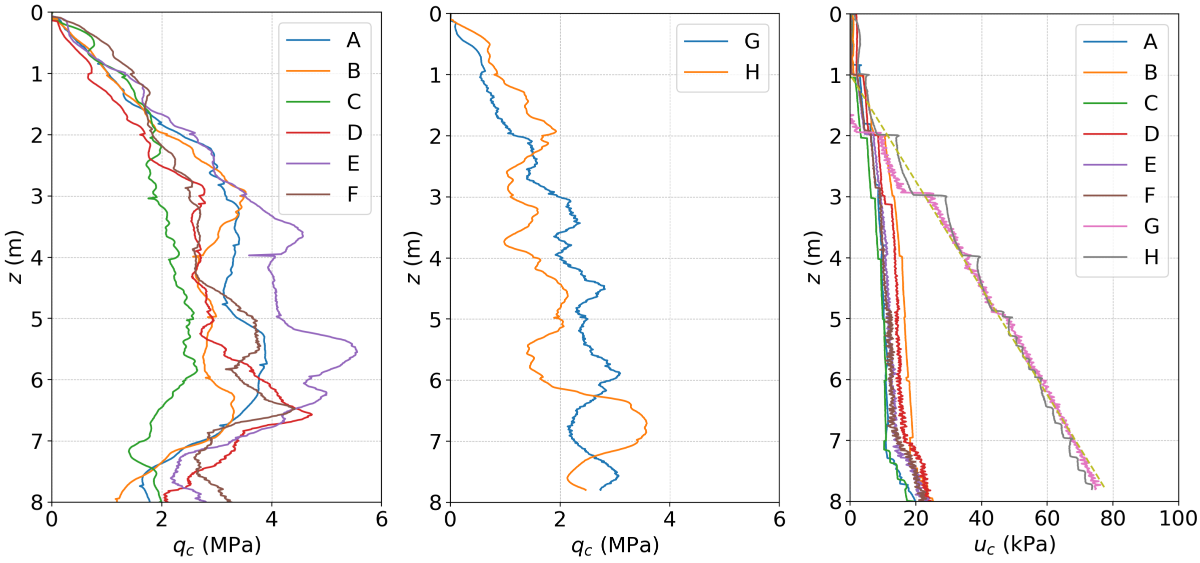

Figure 4-3: CPT results

between CPT locations. This is not always true (particularly for horizontal loading), but is a reasonable assumption for the purposes of producing an approximate model.

Using equation 2.9, the variation of I_D can be found. Assuming first an average unit weight of $\gamma' = 14$ kN/m^3 for the dry case, where $\sigma'_{v0} = \gamma' z$, figure 4-4 left can be derived from CPT E.

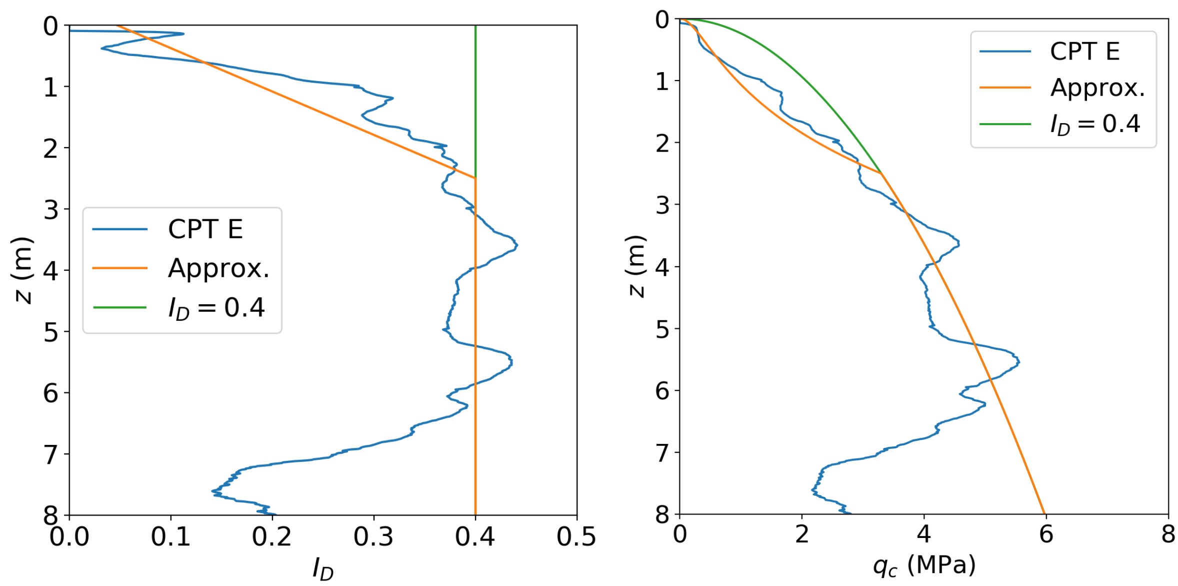

Figure 4-4: CPT found relative density (left) and expected cone resistance from approximated density profile (right)

This distribution is approximated (by the orange line). It consists of a linear region from $I_D = 0.05$ at the surface to $I_D = 0.4$ at 2.5 m depth, and a constant I_D thereafter. Only the region up to ~ 6 m is relevant to the pile testing, so discrepancy at greater depths does not matter. It is assumed to be the same for the wet case, as changing the water level should not alter the soil density.

Along with the data from density testing, the unit weight and hence vertical stress distribution can now be calculated as opposed to estimated (figure 4-5), for both low and high water table cases. Note that re-iterating the new σ'_{v0} into equation 2.9 causes almost no change to the I_D curve, so the approximation holds. Figure 4-4 right shows the back-calculated tip resistance for a sand with the density and stress variations described by the approximation, which agrees well with the actual testing data.

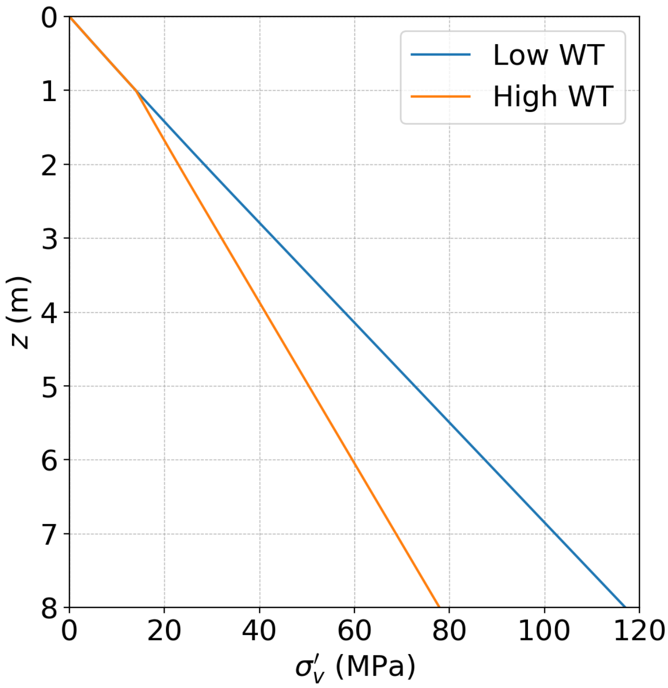

Figure 4-5: In-situ stress distributions

While this approximation of I_D is somewhat arbitrary (it could be said to reach 0.4 slightly earlier or later), the behaviour of the soil is not particularly sensitive to small differences in relative density. It is enough that it follows the trend of q_c well, which is comparable to what a pile will experience. If I_D was assumed to be 0.4 throughout for example, the soil strength would be overestimated by 1.5-3 times at shallow depths (as seen in figure 4-4 left), so the gradual increase is necessary, but its exact form will not lead to large errors.

5 Vertical Performance

5.1 Results

5.1.1 Load Testing

Force-displacement curves for all cases are presented in figure 5-1. The earth pressure data is plotted against displacement in figure 5-2 (sensors 1 to 3 refer to the shallowest to deepest sensors respectively). The earth pressure data for case 4 was found to be unreliable so is not shown. Note case 1 ended prematurely as a result of equipment failure.

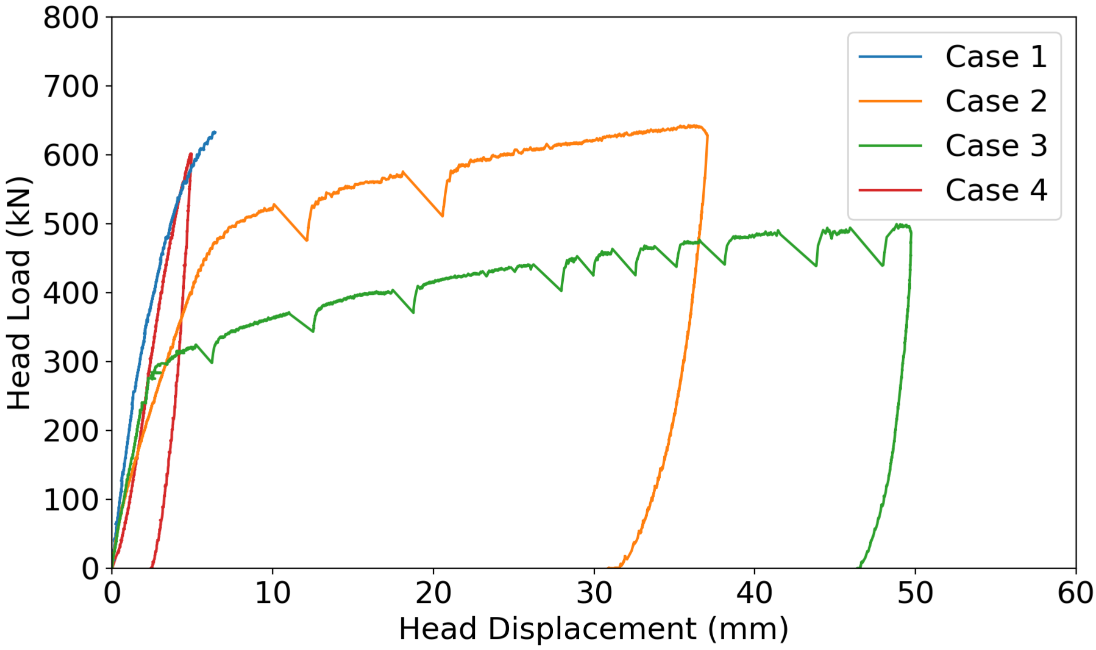

Figure 5-1: Vertical load - settlement response

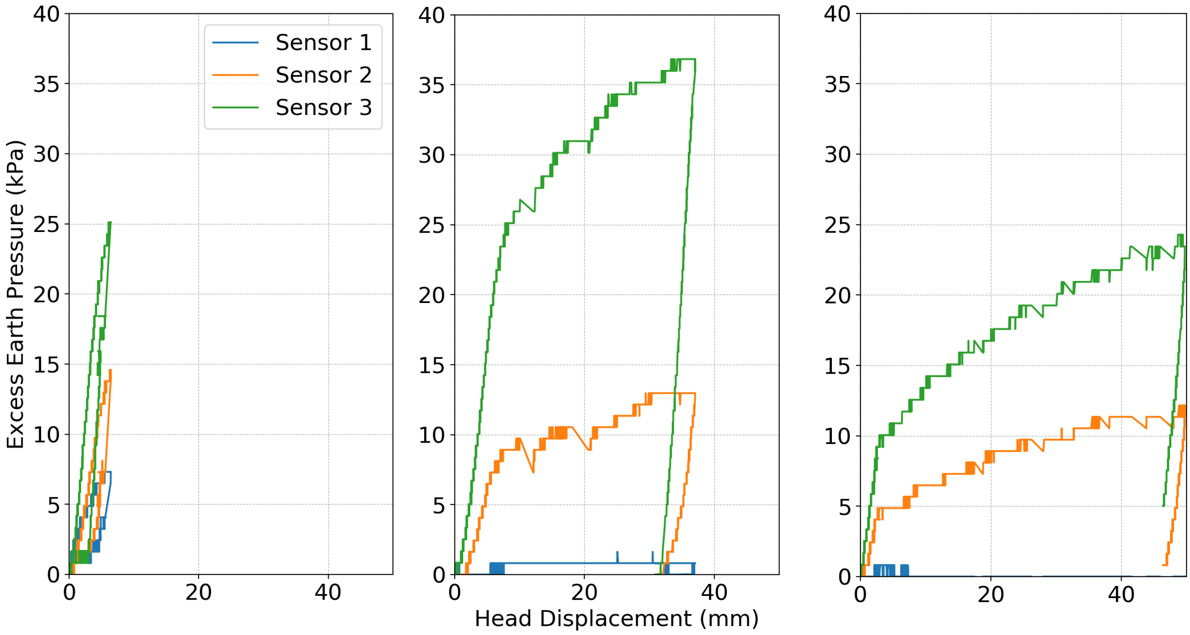

Figure 5-2: Earth pressure - settlement response for cases 1-3 (left to right)

5.1.2 Installation Data

During installation, each surge stroke is effectively a rapid vertical load test, meaning the force data from the piler provides a valuable record of the variation of performance with depth. The raw data for case 1 is provided in figure 5-3.

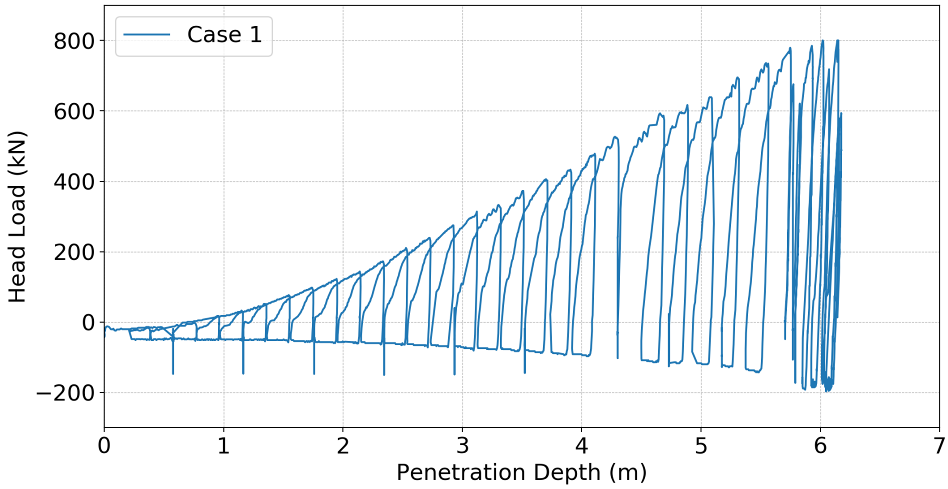

Figure 5-3: Raw penetration force - depth data from piler

There is clearly a constant offset in the force measurement, as it should be zero at the start of installation. This is due to the weight of the piling ram (40 kN) and the pile itself (10 kN), which act in addition to the jacking force. The true load can therefore be found by adding the 50 kN of weight to the recorded jacking force. A second correction to be made concerns the difference in force between penetration (upper envelope) and extraction (lower envelope) strokes at the start of installation. They should begin equally at zero. With minimal soil resistance, the direction of movement of the pile should not affect the force experienced by the jack, yet the downward and upward strokes begin 30 kN apart. This is less easy to explain, but may be down to an internal resistance which only acts in one direction, or systematic error in the measurement system. Either way, it is unphysical and hence corrected for by reducing the force in downward strokes by 30 kN.

The corrected installation data for the three individual piles is shown in figure 5-4. Note that the regions close to the final depth for cases 1 and 2 are slightly anomalous - measurement issues relating to the piler condition being altered (for example, from automatic to manual) mean that data from these regions will be dismissed. The earth pressure data is shown in figure 5-5. The corrected installation data for the three piles of case 4 is plotted in figure 5-6. The central pile was installed first and is shown on the left. It is seen that the maximum force criteria was increased from 300 to 350 kN part way through the second pile installation.

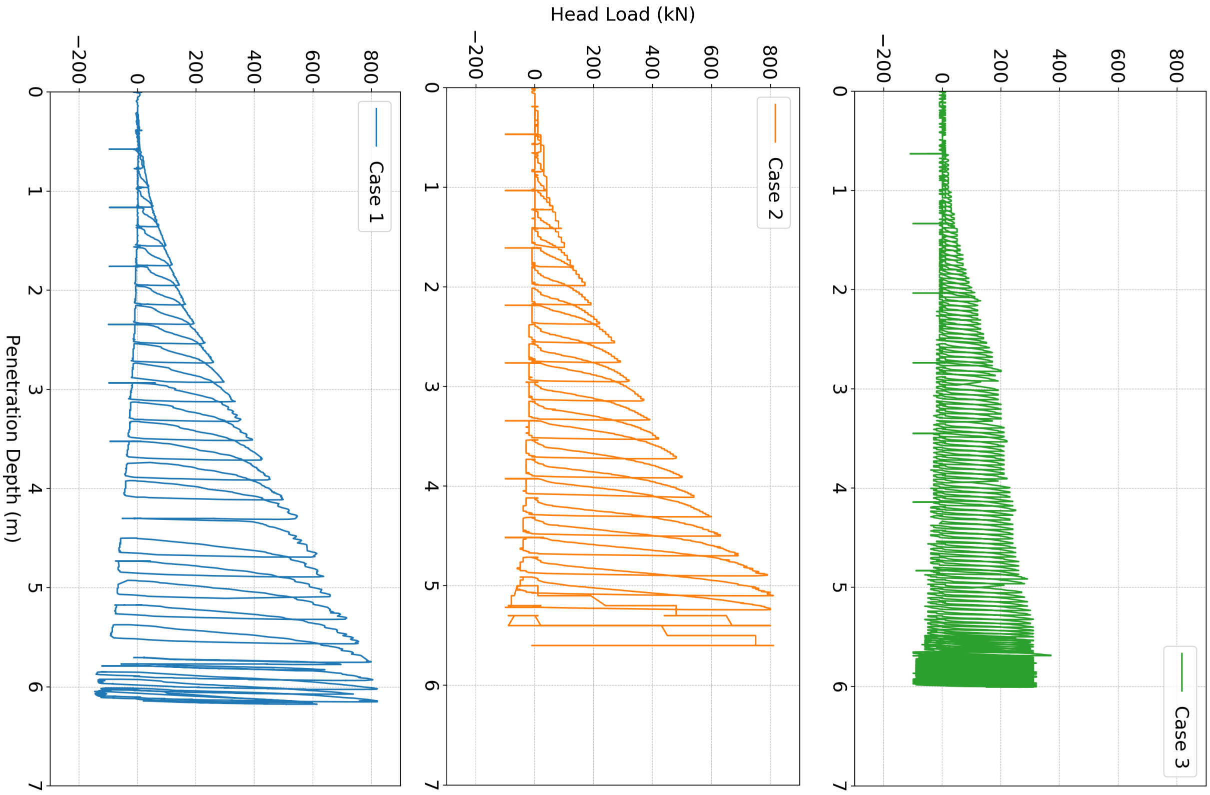

Figure 5-4: Corrected penetration force - depth data from piler

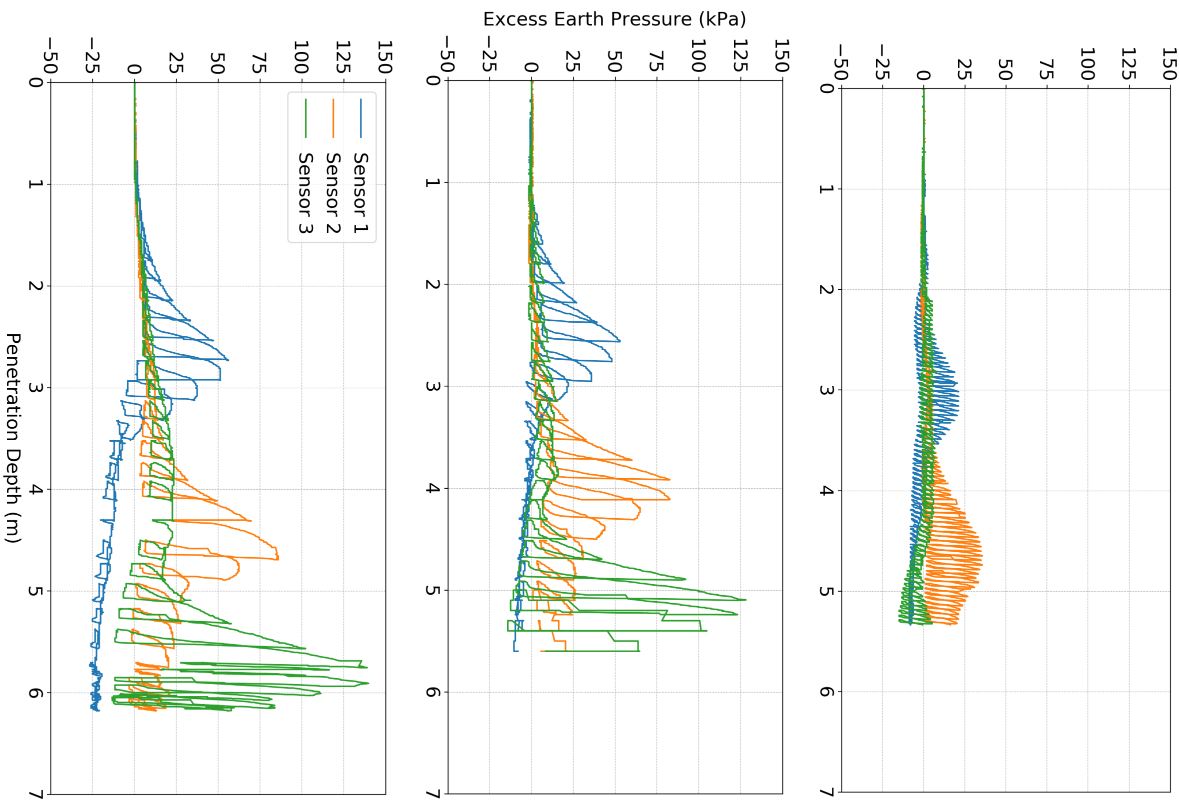

Figure 5-5: Earth pressures during installation for cases 1-3 (left to right)

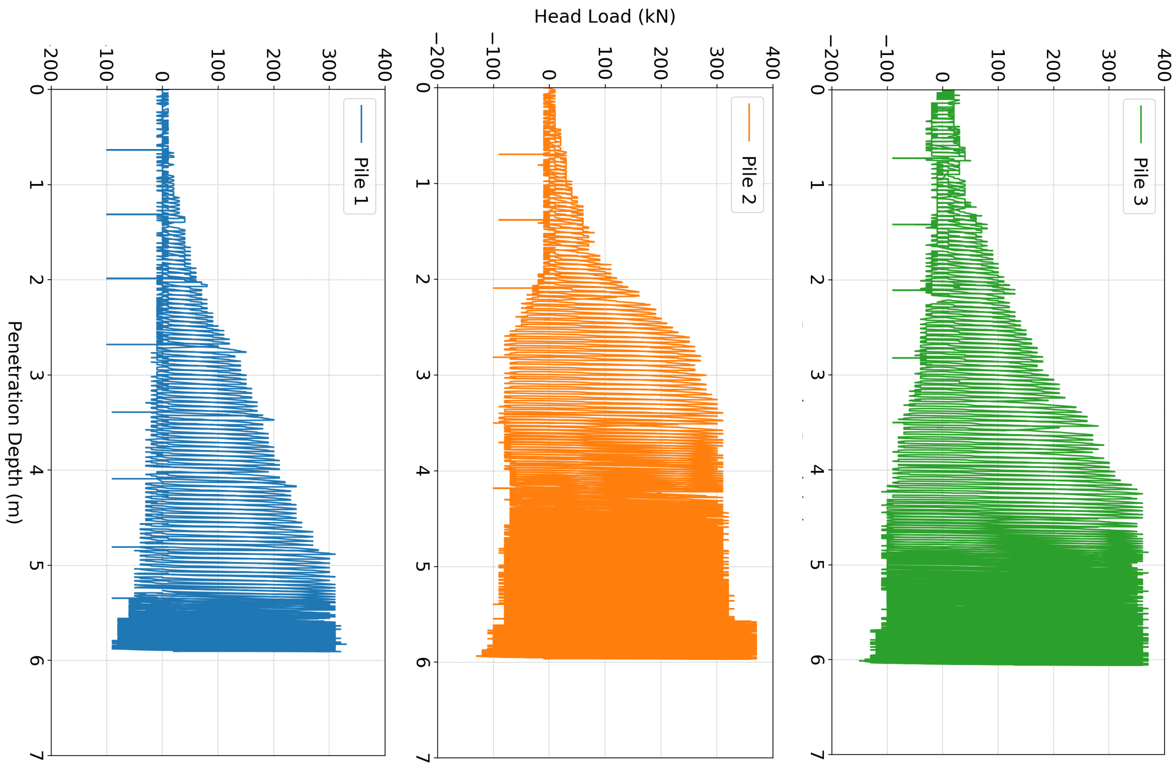

Figure 5-6: Corrected penetration force - depth data from piler for case 4

5.2 Analysis - Individual Piles

5.2.1 Shape of Response

The load-displacement curves in figure 5-1 exhibit two clear regions, a stiff initial response, and a subsequent ‘yielded’ region characterised by low stiffness and instability (the piles undergo multiple sudden, large deformations or ‘slips’). The former can be considered an elastic region, and the latter plastic. Not only is this intuitive, it is supported by the displacements regained in the unloading region for cases 2 and 3 (5.5 and 3.2 mm respectively) being very well aligned with the displacements at the respective yield points (i.e. the elastic deformation), though these cannot be pinpointed as precisely.

The yield is considered the appropriate point for the design capacity of a pile. To ensure robustness, applied loads should be limited to this level, preventing cumulative deformation from repeated loadings and eliminating the possibility of damaging ‘slips’. As such, the content of this section will focus on estimation of the yielding load. Since the displacements within the elastic region are well within the $D_{eq}/10$ limit (at most 1.6% and 0.7% of D for cases 2 and 3), this is a problem governed by strength and not stiffness, and analysis will follow accordingly.

The shapes of the load-displacement characteristics are evidently similar. In figure 5-7, the graphs of all three cases are scaled with respect to their yield points. There is an undeniable likeness between cases 2 and 3, which suggests that the installation regime only acts to scale the response, but not change its shape. This is notable as it provides the means to estimate the ultimate load from the yield. From case 3, there is a factor of 1.65 relating them. It is not clear whether this value is a specific function of the pile geometry, or a more universal correlation. Only a limited picture of case 1 is available, although by mapping it to the other curves using a 'guessed' yield point, an estimate for the true yield can be produced - $V_y = 650$ kN.

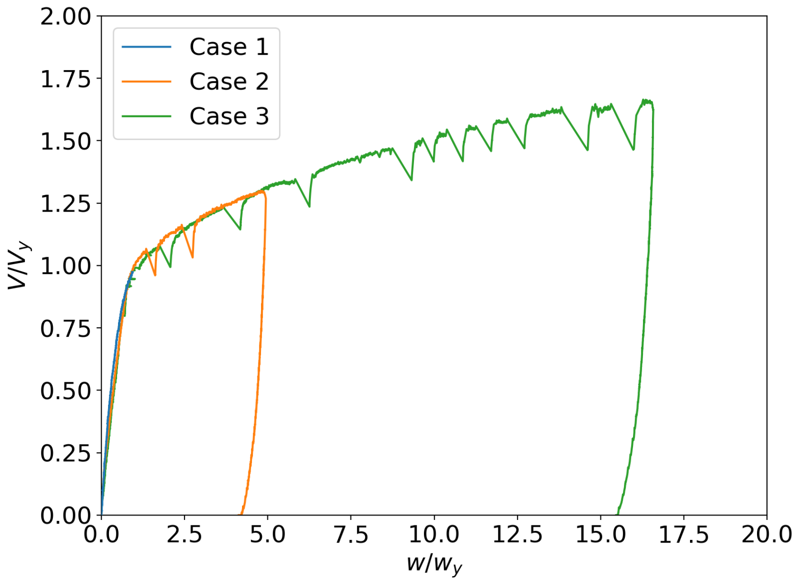

Figure 5-7: Normalised vertical load test responses

5.2.1 Comparison with Installation Data

The vertical load tests were performed after unloading from the final penetration stroke, effectively being the next load cycle (though without the extraction stroke). It is therefore useful to plot the results against the last installation cycle for which there is reliable data in each case (figure 5-8). In terms of load, there is an almost striking agreement between the yield points and the points at which the lines from consecutive cycles cross (hereafter referred to as cycle intersections). It is useful to first consider the physical significance of this cycle intersection.

At the end of any surge cycle, a pile has reached its maximum depth d. Crucially, the pile must be in the yielded region; otherwise, no net penetration would have been made during the cycle. It is then unloaded, and the elastic displacement lost. Naturally, for the pile now to progress further than d it must yield (elastic deformation can take it back up to d but no further). From figure 5-8, the cycle intersection corresponds to the point at which the pile

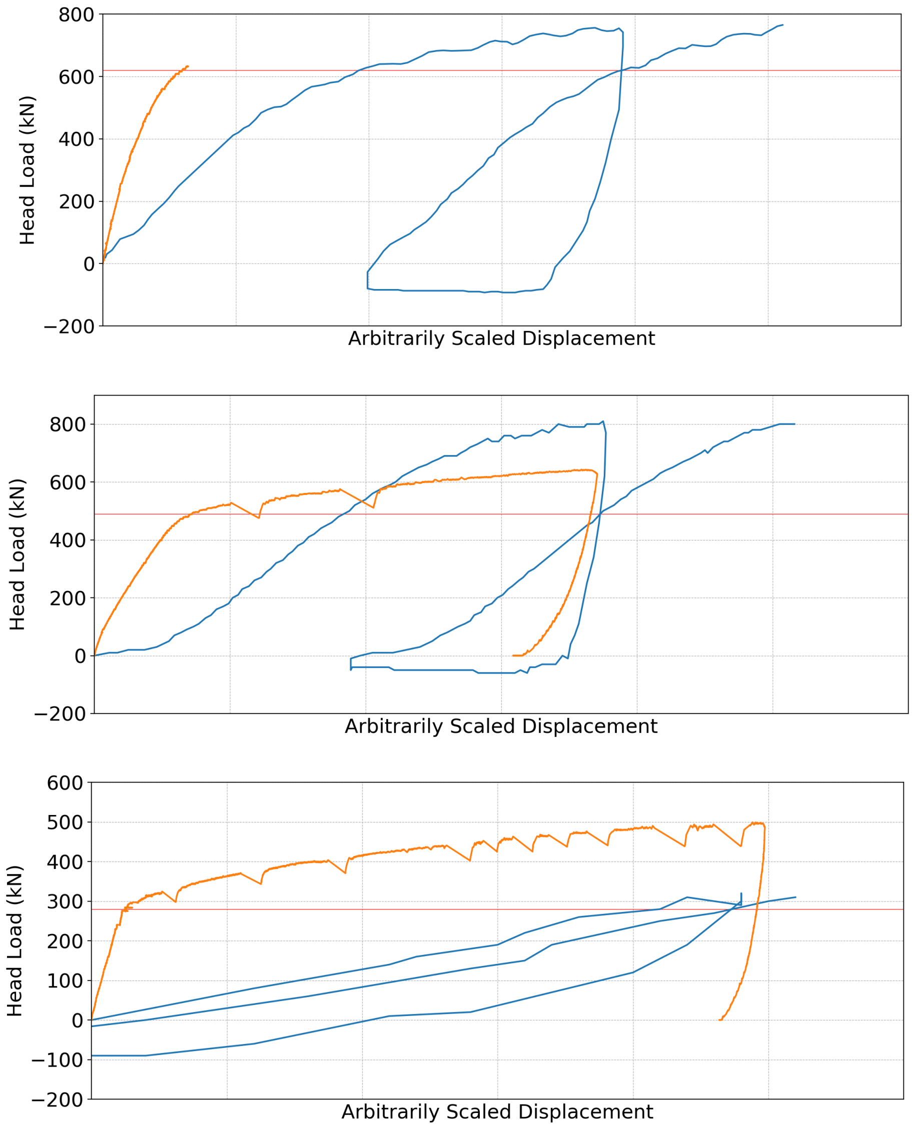

Figure 5-8: Comparison of load tests and final installation cycles for cases 1-3 (top to bottom)

returns to d after a surge cycle (it is slightly less than d in reality but the difference is small since the unloading curve is steep), and as such, represents the yield point for the next cycle. The force at d is now lower due to the effect of the surging, but still the soil must yield for further plastic deformation (i.e.penetration) to occur.

The fact that the yield and cycle intersection align so well suggests that only the unload portion and not the full surge cycle is required for the reduction in force from one cycle to the next, as only this happens between installation and load test. There is further evidence to support this. During the installation for case 1 at 4.3 m of penetration, the full extraction stroke is not carried out (figure 5-4). Despite this, there is no doubt that the same pattern is followed - the force curve is made significantly lower than the previously, and the yield point of this new curve is roughly in line with the adjacent, full cycles.

The observations here lead to an incredibly significant result. Once installed, the design capacity of the pile can be assessed easily and accurately by looking at the installation data. Since the required data is recorded automatically by the piler, 'zero-effort' experimental verification of the design resistance is carried out by default. The pile must still be designed in the first instance of course - relevant analysis will be covered in the next section. Before proceeding, best fit curves for the cycle intersections, detailing the evolution of yield point with depth, have been produced for cases 1-3 (figure 5-9). The recurring outliers in case 2 have been ignored for the best fit - they all occur after a change in piler position so are deemed subject to systematic error.

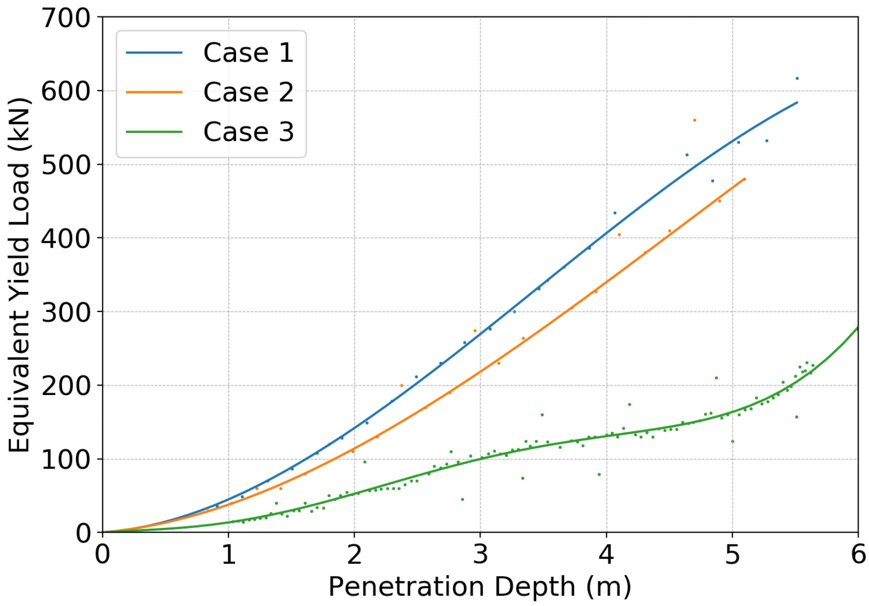

Figure 5-9: Cycle intersection variation with depth

5.3 Capacity Model

In this section, a theoretical model for the prediction of pile capacity without installation effects will first be prescribed. This value should then be adjusted to account for installation effects, where the level of adjustment is determined empirically, as the stress history is too complex to model. The reason for this semi-theoretical approach is that the shape of the vertical load characteristic is independent of the specific installation (figure 5-7), so it would make sense to characterise the vertical behaviour by a universal model. This can then simply be scaled to incorporate installation effects.

For all cases, figure 5-4 shows a much larger penetration force (upper envelope) than extraction force (lower envelope). This seems counter intuitive. Typically, the former represents the sum of the base resistance and skin friction, and the latter just the skin friction

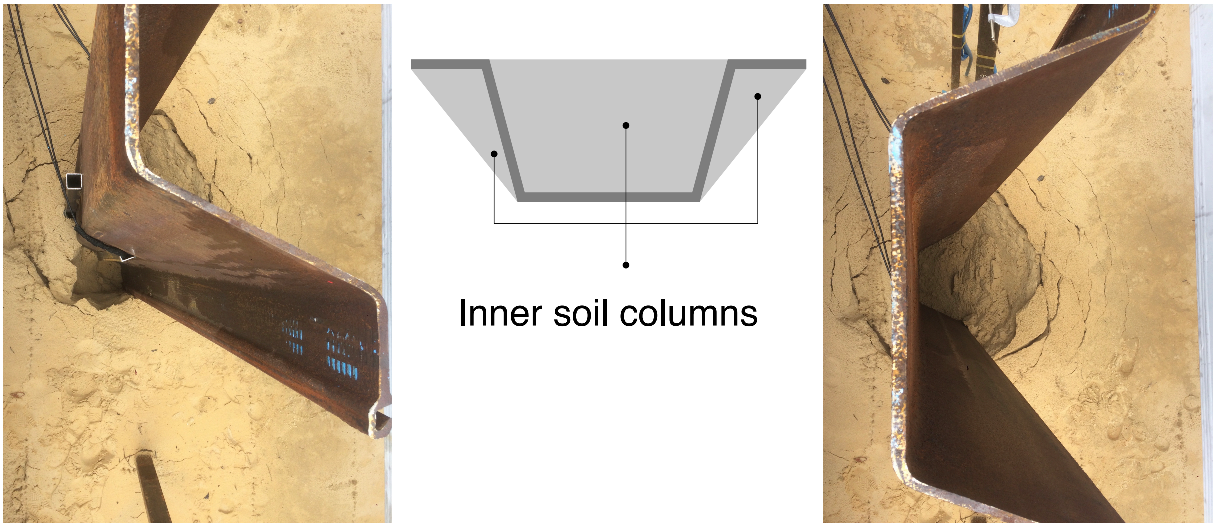

Figure 5-10: Gross area effects of sheet pile

(which should be equal in both directions), but for a thin-walled sheet pile, the base area is negligible compared to the shaft area. The pile must therefore be able to utilise some of its gross base area on downward penetration, via some form of vertical arching and/or plugging In fact plugging was observed during the later stages of installation for all piles (figure 5-10).

5.3.1 Unplugged Model

Following from section 2.3, a small element of the inner soil column can be considered as a free body (figure 5-11). This differs from the tubular model in that there is a length l_p on which it experiences downwards shear from the pile, but also a length l_s where it experiences upwards resistance from the external soil.

Since there is sliding at the pile wall, equation 2.4 gives $K = 0.59$, with $\tau_p = K\sigma_v' \tan\phi'$. Determining τ_s is trickier. In the unplugged mode there is no sliding at the external interface, meaning the mobilised friction angle may lie anywhere between 0 and ϕ'. It will depend on how the downward forces are shared between plug compression and external shear, which is too complex to model. For now, let us express it as $\tau_s = \chi_{mob} \cdot K\sigma_v' \tan\phi'$ where χ_{mob} varies between 0 and 1. Integrating the equilibrium of forces yields:

$$\sigma_v' = \frac{\gamma' A_g}{(l_p - \chi_{mob} l_s) K \tan\phi'} \left(e^{\frac{(l_p - \chi_{mob} l_s) K \tan\phi'}{A_g} z} - 1 \right) \qquad (5.1)$$

This is equivalent to the expression for a tubular pile, but with $l_p - \chi_{mob} l_s$ replacing πD and A_g replacing $\pi D^2/4$. There is another difference that must also be considered. For a tubular pile, there is no limit to the amplification of stress. For a sheet pile, the horizontal stress is

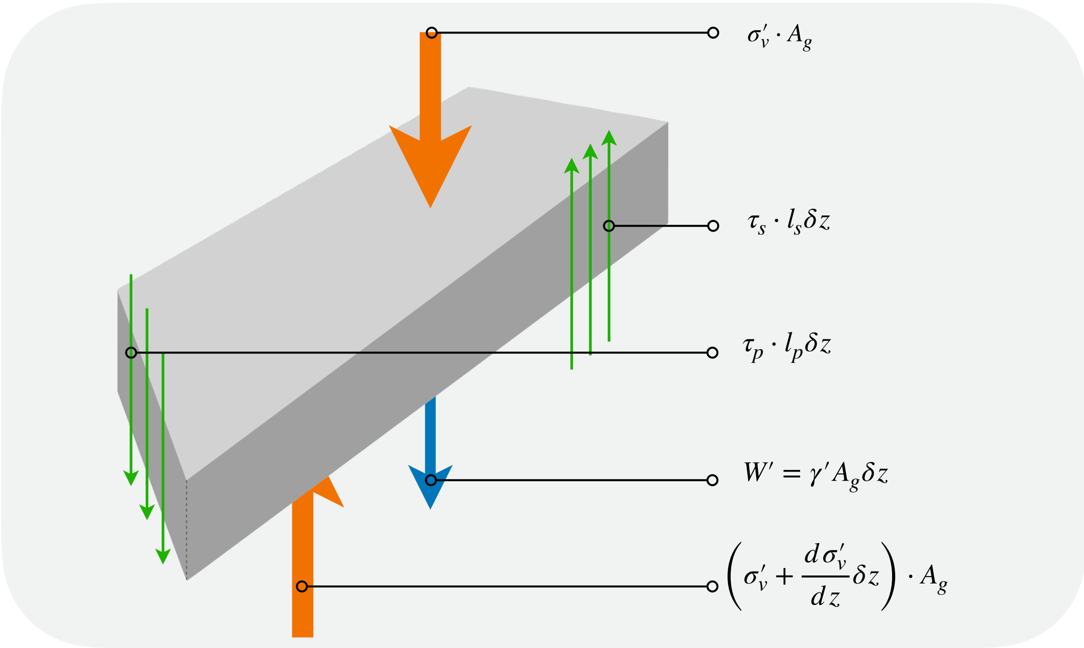

Figure 5-11: Sheet pile vertical arching

limited to the maximum pressure that the external soil can provide - it is assumed that this is equal to the maximum lateral earth pressure $K_p^2 \sigma_{v0}' = 9.52\sigma_{v0}'$ (section 2.4). This will eventually be reached at a critical depth. Below this, it must be that $\tau_p = K_p^2 \sigma_{v0}' \tan \phi'$.

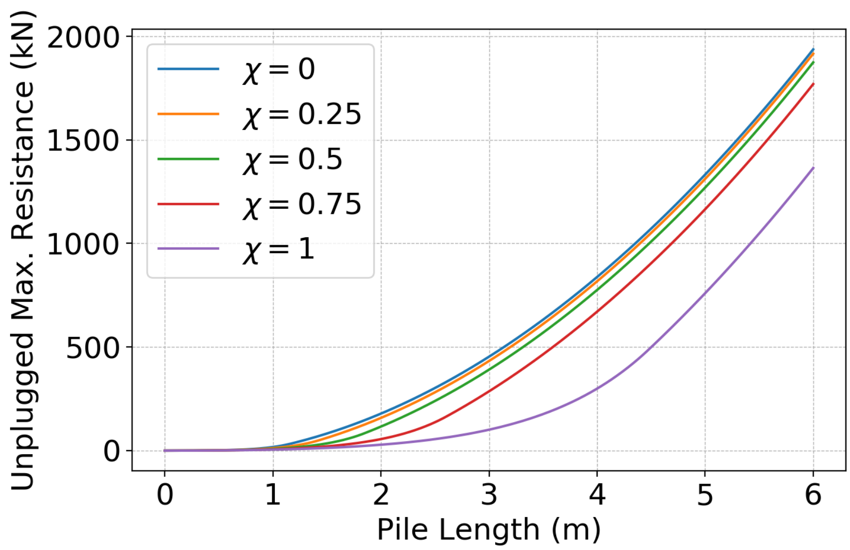

Figure 5-12:Variation of Q_{upl} with χ_{mob}

$V_{max,plugged}$ can then be found by numerically integrating $\tau_p l_p = \sigma_h' \tan \phi'$ along the piles length, where σ_h' is the minimum of $K_p^2 \sigma_{v0}'$ and K times equation 5.1. This is plotted for multiple values of χ_{mob} in figure 5-12. For the majority of the range the curves remains close to that of $\chi_{mob} = 0$. Additionally, it is likely that $\chi_{mob} = 0$ close to the surface (low shear stresses from the pile are easily 'absorbed' by the axial compression before reaching the external soil wall) and $\chi_{mob} = 1$ at the transition to a plugged mode (since the external interface undergoes sliding at this point).

5.3.1 Plugged Model

For the plugged mode, where the entire gross area moves down together, penetration force is governed by the end bearing capacity. This is calculated for various depths using the method described in section 2.1. The shape factor is calculated by approximating the trapezoidal gross area as an equivalent rectangle (760 x 300 mm). The base resistance must be transferred to the pile via skin friction, and from figure 5-13, it is seen that it is in fact amplified by the external soil resistance.

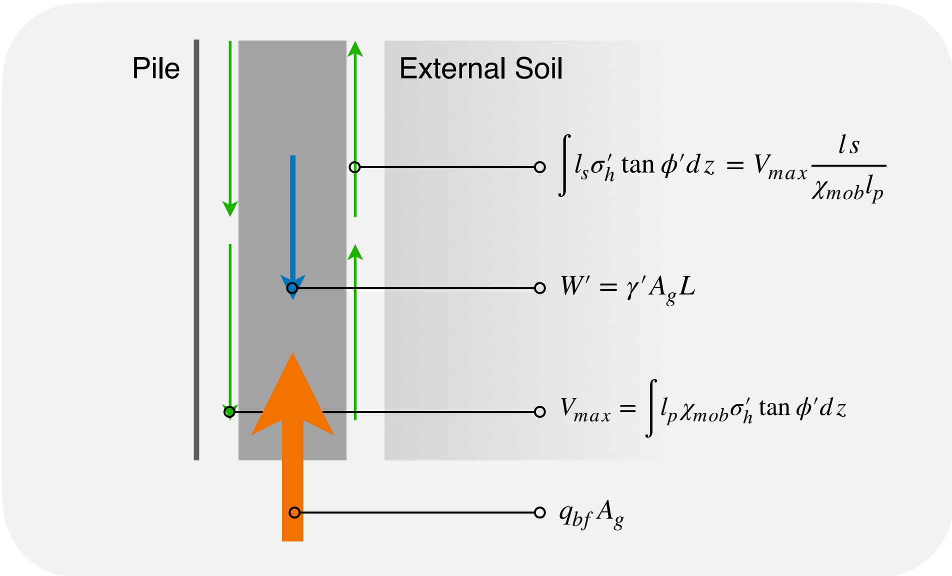

Figure 5-13: Plugged mode equilibrium

Conversely to before, for this mode it is not known how much of the pile friction is mobilised as there is no slip on the pile-soil interface. However, it is fair to assume that the soil is close to fully mobilised, since it must be at the point of transition from the unplugged mode (where sliding occurs), and it leads to the lowest V_{max} (i.e penetration is more favourable for higher χ_{mob}). For $\chi_{mob} = 1$, the head load is related to the base resistance as follows:

$$V_{max,unplugged} = \frac{l_p}{l_p - l_s} \cdot A_g(q_{bf} - \gamma' L) \tag{5.2}$$

5.3.1 Comparison with Results

By multiplying the yield point curves of figure 5-9 by 1.65, estimates of the the ultimate load are obtained (section 5.2.1). These are plotted in figure 5-14, separated into high and low water table cases, against the model predictions.

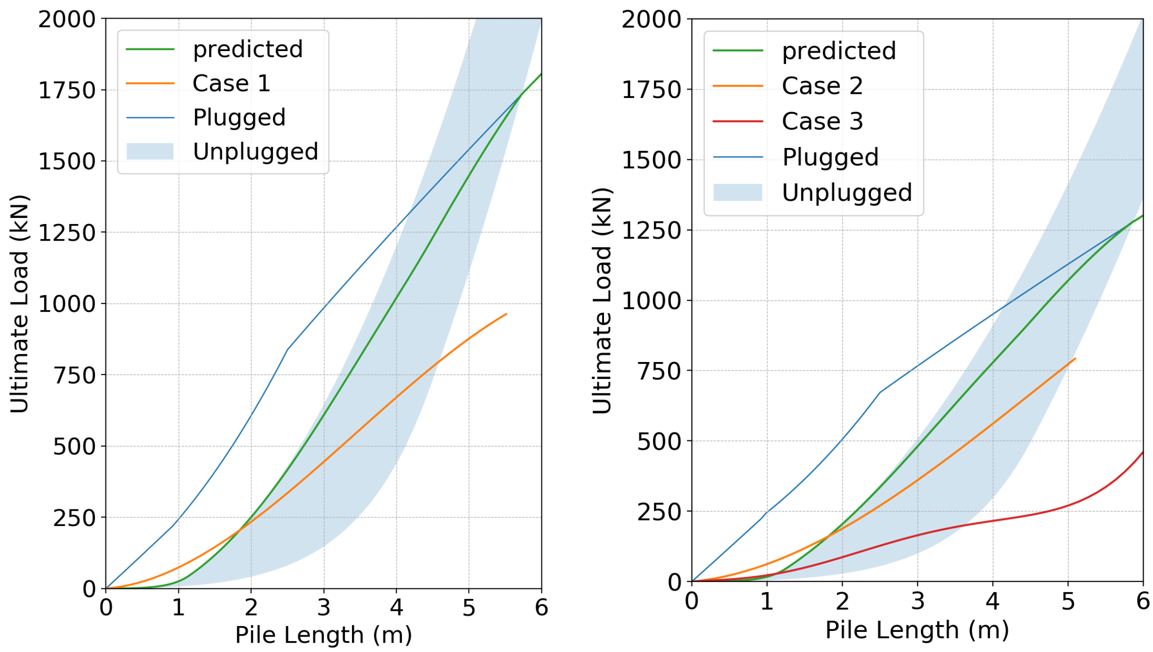

Figure 5-14: Comparison of model predictions and recorded data

The unplugged mode is plotted as a likely path within an envelope bounded by limiting values of χ_{mob}. This is based on discussion above suggesting χ_{mob} starts at 0, reaching 1 when the transition to plugged occurs, with the line staying close to $\chi_{mob} = 0$ for the majority. It is therefore only approximate. Since equation 5.1 is only possible with constant γ', average unit weights (9.9 and 14.6 kPa for dry and wet respectively) over the depth have been adopted. For the horizontal limit pressure and plugged capacity, the in-situ stresses and densities as found in section 4.2 are used. Friction on the length pile surface not in contact with an inner soil column has been neglected, since this length is fairly small, and 'normal friction' is observed to be very small from extraction loads (figure 5-4).

The theoretical and experimental curves follow the same trend, and the model tends to overestimate more for greater depths. This is expected, as the amount of surging experienced increases as the pile is installed further. There are a few key discrepancies however, which should be addressed. Firstly, this incorrectly suggests that the onset of plugging occurs near the end of pile installation for all cases, when in reality 1-2 m of plug depth was observed. This may be partially explained by the fact peak friction was neglected in the unplugged model, or that the true limit pressure is higher than $K_p^2\sigma'_{v0}$ due to full interface roughness (which may not be the case for the model tests - section 2.5); these would push the true curve upwards bringing the transition earlier. There is also an underestimate at low depths. Again, peak friction, the 'normal' friction and steel area end bearing which have been ignored would rectify this gap somewhat, though this error is relatively insignificant as the depths are well below any practical pile length.

The overestimation is greater for case 1 than 2, when they have identical surging regimes. This is thought to be the result of partially undrained behaviour in case 2's saturated soil. To demonstrate this possibility, an order of magnitude calculation can be performed by considering 1-D consolidation along a drainage path of approximate length $L = 6$ m. For a typical sand with $k = 10^{-4}$ m/s and $E_0 = 40$ MPa, $C_v = kE_0/\gamma_w = 0.4$ m^2/s. The time for a single downward stroke being 6.15 s, $T_v = C_v t/L^2 = 0.07$ and $R_v = 0.3$, meaning pore pressures generated during a stroke are far from dissipated over the course of that same stroke. While a very crude calculation, it highlights the possibility of undrained effects. Since dilatancy is likely (peak friction was observed in bearing capacity calculations), this would lead to increased soil strength, and higher measured loads for case 2 as seen.

Additionally, the model is supported qualitatively by earth pressure readings. Spikes of horizontal pressure significantly greater than the in-situ stresses (up to $2\sigma'_{v0}$ added) are seen. This is unexpected for vertical loading, though makes perfect sense in light of the amplification of plug stresses causing high pressure on the external soil walls (the external boundary of one of the triangular columns points towards the earth pressure sensors).

This model is not perfect. The nature of the stress fields developed within the soil are inherently complex given the arbitrary geometry of a sheet pile, and this model attempts to simplify these matters into a more easily understandable form. In doing so, it still manages to agree well with experimental observations, and provided a suitable method for taking into account installation effects is possible, it may provide an accurate depiction of sheet pile behaviour.

5.4 Installation Effects

It will be difficult to produce an accurate method for quantifying the effect of surging from the obtained results. In addition to the limited data, there are a large number of variables which affect the amount of strength degradation. For example, not all cycles will be equal - a cycle at 10 m penetration depth will contribute toward more friction fatigue than an equivalent cycle at 1 m. The interaction between surging regime and capacity is clearly complex. However, an eventual design method should provide a simple way to incorporate installation effects, and this section will attempt to point towards a method of doing so using a simple reduction factor to the maximum capacity.

It has already been seen that the most significant part of a surge stroke is simply the unloading. The instances presented as evidence are isolated cases, and should not be generalised to say that unloading/reloading would be equivalent to full surging if used throughout the installation regime. They do suggest however, that the existence of a surge cycle is of much greater importance than its magnitude. Based on this, it is theorised the number of cycles is an appropriate indicator for the capacity loss. Figure 5-15 gives the reduction factor $F_{surge} = V_{max,measured} / V_{max,predicted}$ from the graphs in figure 5-14, as a function of the number of cycles.

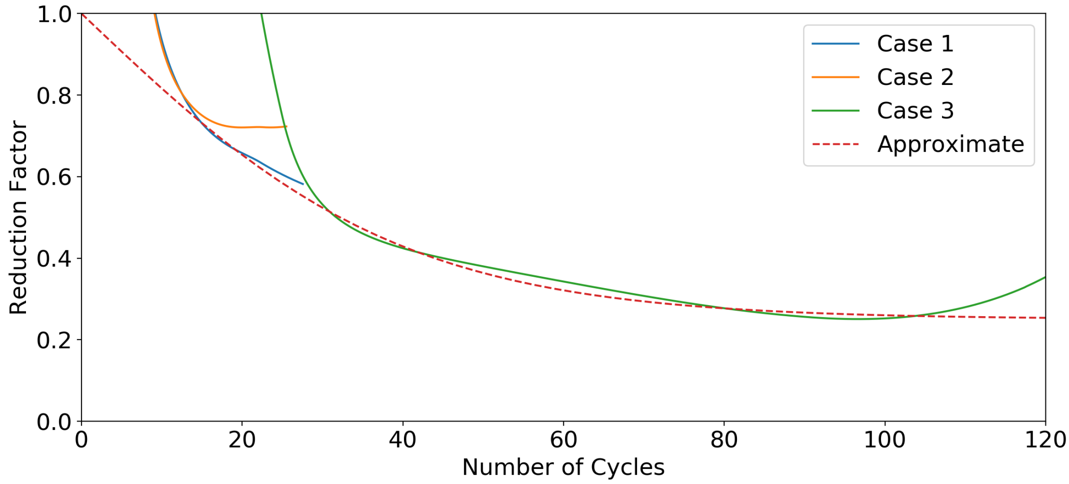

Figure 5-15: Reduction factor variation with surging cycles

The number of cycles has been calculated using the initial installation criteria, so doesn't account for the reduced stroke lengths towards the end of the installations. The model is not perfect, and as mentioned only approximate due to the true unknown distribution of χ. That being said, ignoring the initial region where the capacity model underestimates, there is potentially a smooth function for the reduction factor (the dotted line is one such hyperbolic curve), which seems to reach an eventual equilibrium at $F_{surge} = 0.25$ (i.e. the loss of capacity due to friction fatigue above the pile base being balanced by the increase in capacity from added length). The curve for case 3 strangely increases at the end, as the stroke lengths shrink ever smaller and smaller. This is in agreement with Burali d'Arrezo's hypothesis that a small enough surge length can actually increase capacity. It is sensible to ignore this region for the purposes of normal design, though it does lead to the idea that tight surging could potentially be used for capacity increase after installation. This will not be considered here.

This report will restrain from analysing any results too deeply as confidence in these curves is not particularly high, considering the size of the data set against the complexity of the problem. Defining F_{surge} as a function of the number of cycles is simply an example of how the phenomena may be taken into account in design using what is deemed to be the most significant factor during installation.

5.5 Analysis - Grouped Piles

5.5.1 Installation

Given that the surging parameters were equivalent to case 3, similar curves would be expected. The first pile does follow the same trend as in case 3, though the 2nd and 3rd differ (figure 5-6). It is proposed that this difference is dominated by the interlock friction and not other boundary effects. On first look, the discrepancies in penetration force seem to be mirrored in extraction force (the additional force seems to be independent of direction, but it has been observed that soil resistance is not), and are very different for the 2nd and 3rd piles (which should behave equivalently). Furthermore, figure 5-16 (detailing a few cycles for pile 2) shows that a large resistance is mobilised immediately on change of direction, uncharacteristic of soil but expected for pure friction. This is not seen for pile 1.

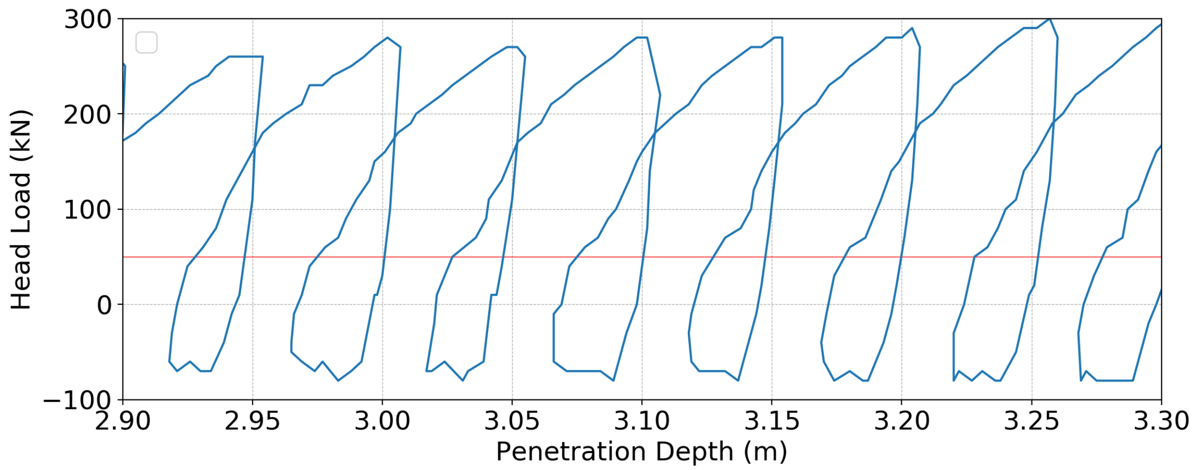

Figure 5-16: Immediate mobilisation of resistance on reversal

In figure 5-17, the increases in extraction envelopes from pile 1 to piles 2 and 3 (hypothesised as the interlock friction) have been subtracted from their respective penetration force curves. The resulting envelopes are now much closer to that of pile 1, suggesting the additional force is indeed bi-directional, and therefore likely to be interlock friction. Estimation of the required penetration force would hence be the same as for an individual pile, but with an additional friction term. This will depend on the pile and would require more data to estimate confidently, but from the differences in extraction force, here it is of the order of 10 kN/m, subject to random fluctuation.

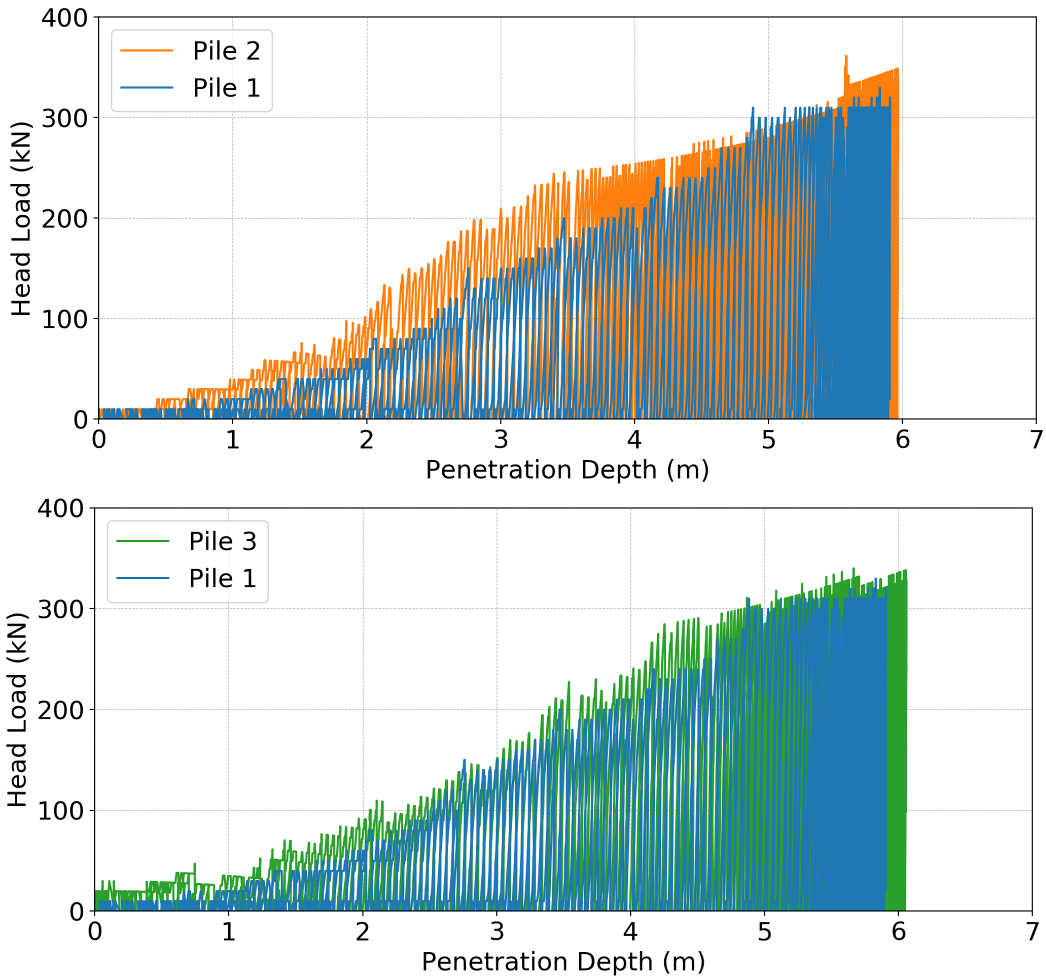

Figure 5-17: Pile 2 and 3 penetration forces adjusted for interlock friction

5.5.2 Vertical Response

In figure 5-1, the initial low stiffness is a result of indeterminacies in the applied loading. Small differences in level between pile heads mean the load is not initially applied through all of them. It soon engages all piles, and the higher combined stiffness is reached. In estimating capacity, the same unplugged and plugged mechanisms can be evaluated for the group, with new geometric parameters. The gross area in figure 5-18 is assumed, and the resulting predicted capacity is compared with the individual case in figure 5-19.

At a length of 5.84 m, the plugging mechanism governs by a wide margin, with an ultimate head load of 2203 kN. Assuming the same installation degradation as for case 3 (since all piles were installed in the same manor, this is multiplied by 0.354 to give $V_{max} = 779$ kN. Finally, this would correspond to an approximate yield of $779/1.65 = 472$ kN. This is overly conservative, as the piles remain in the elastic region even at 600 kN, though there are signs of softening; perhaps it was to yield soon after.

Figure 5-18: Gross section for pile group loading

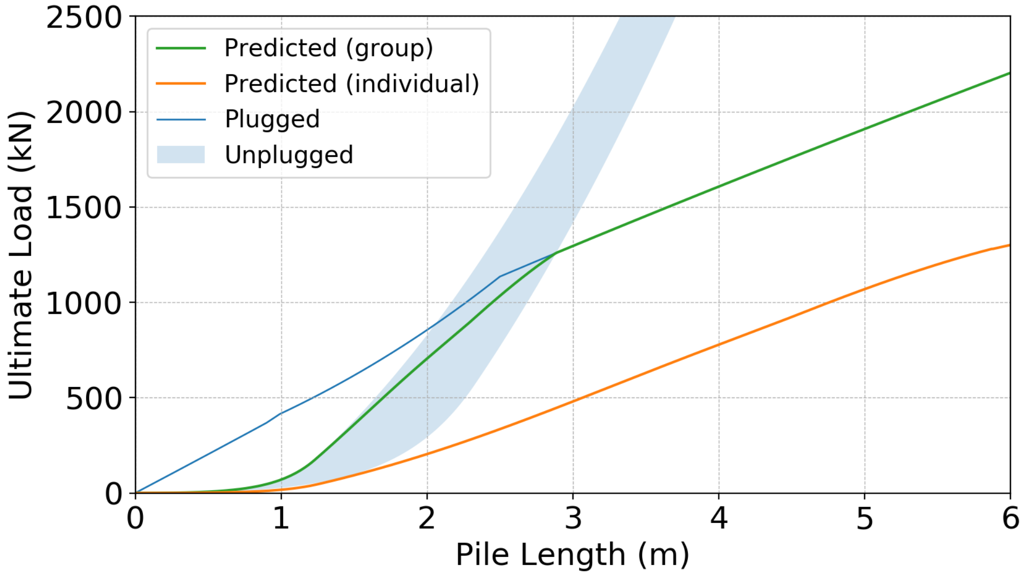

Figure 5-19: Group vs individual response using proposed model

It is not surprising that it incorrectly estimates the yield due to the nature of assumptions made. Most prominently, the surging on each individual pile has been assumed to have the same effect on the group of piles as a whole, and similarly the load displacement curve has been assumed to have the same shape as that of an individual pile, despite very different geometries. Still, the method is able to produce a conservative estimate that is likely to be within the correct order of magnitude. This leads credence to its potential use as part of a design method. The same theoretical model could be used for individual and group piles, since the group effect is adequately modelled by changing the parameters. More evidence would be required however to refine the model to account for installation effects on group behaviour, and to reduce its conservativeness.

6 Horizontal Performance

6.1 Results

Force-displacement curves for all cases are presented in figure 6-1. The displacement is measured at the point of loading. Case 1 having the low water table and case 4 being the group test, they are naturally stiffer than cases 2 and 3.

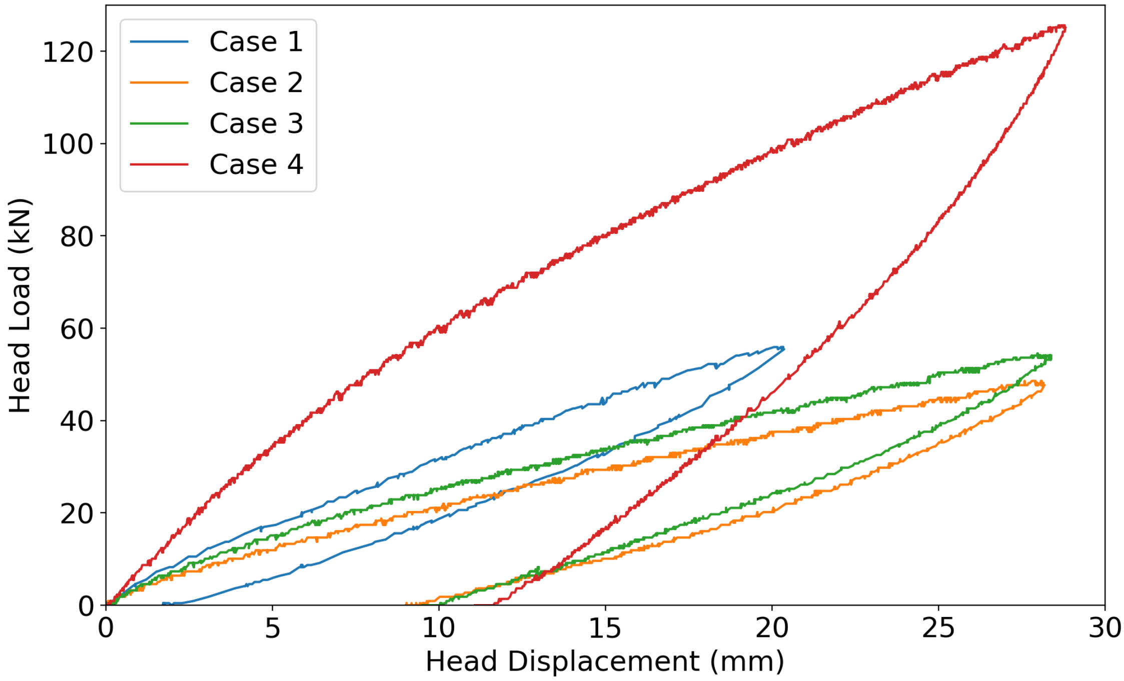

Figure 6-1: Horizontal load - deflection response

The P-y extraction process (section 3.4.1) was also carried out for seven loads in cases 2-4. Case 1 was exempted - due to complications in the testing resulting in multiple loadings and hence cyclic loading history, the inclinometer data was found to produce less reliable results. Curve fits were applied to the bounded regions for deflection and pressure; an example is shown in figure 6-2. These fits are of course only one path within the bounded region, and hence do not necessarily reflect the true behaviour, though are used as representative as a single curve is needed for meaningful analysis.

For the lower loads (such as that in figure 6-2), the output is less reliable. It is unphysical that the depth of zero deflection is different to that of zero pressure. However, while the intercepts of the deflection plots vary, the pressure plots follow more similar trend throughout all levels of loading - the shapes remain similar but they increase in magnitude. For this reason the deflection fit (orange) is ‘corrected’ by matching the intercept with the point of zero pressure.

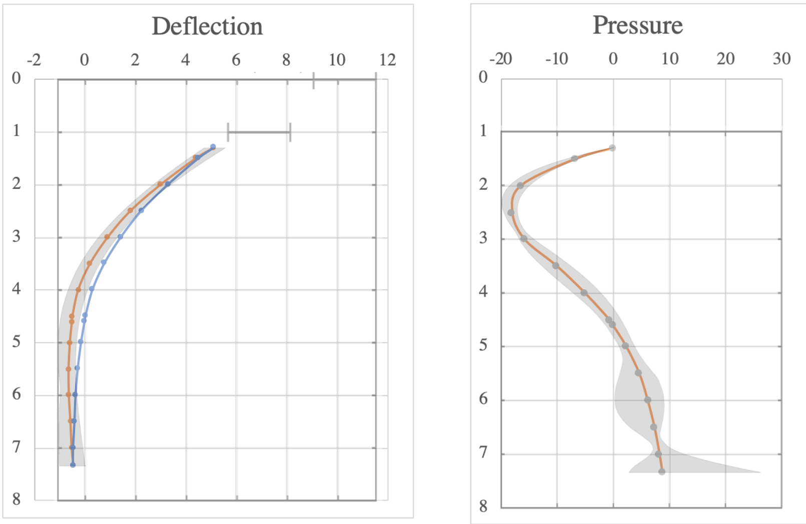

Figure 6-2: Probfit output curve fitting

The corrected curve (blue) is an interpolation between the measured data and a straight line between the top and bottom deflections, such that the intercept is in the right position. All corrected displacements and pressures are plotted in figure 6-3.

P-y curves can be extracted from these and compared to the literature at each depth that the curve fits are prescribed. This has been done for three shallow depths for each case in figure 6-4 (the modified P-y curves will be explained in section 6.2.2). At greater depths, the deflections are small compared to the ranges of the bounded regions, hence the resulting curves are unreliable.

6.2 Analysis - Individual Piles

6.2.1 Shape of Response

Unlike during the axial tests, the piles were seen to reach the deflection limits well before their ultimate loads. In all of the tests, there is no sign of the capacity being approached (the lines remain approximately straight) when the maximum allowable deflection is reached or approached. For this reason, the problem of lateral design for sheet piles is considered primarily one of stiffness and not of strength. As sheet piles tend to be much more flexible than tubular piles, this is not entirely surprising.

For all cases there is an initial high stiffness region, before some of this stiffness is lost and the response becomes approximately linear. This behaviour is unusual, as the degradation in stiffness is very sudden, rather than a more gradual reduction as might be expected. Cases 2 and 3 in particular are the most useful to compare. The pile in case 1 is obviously stiffer due to the higher in-situ stresses in the soil, but for cases 2 and 3 the soil conditions are

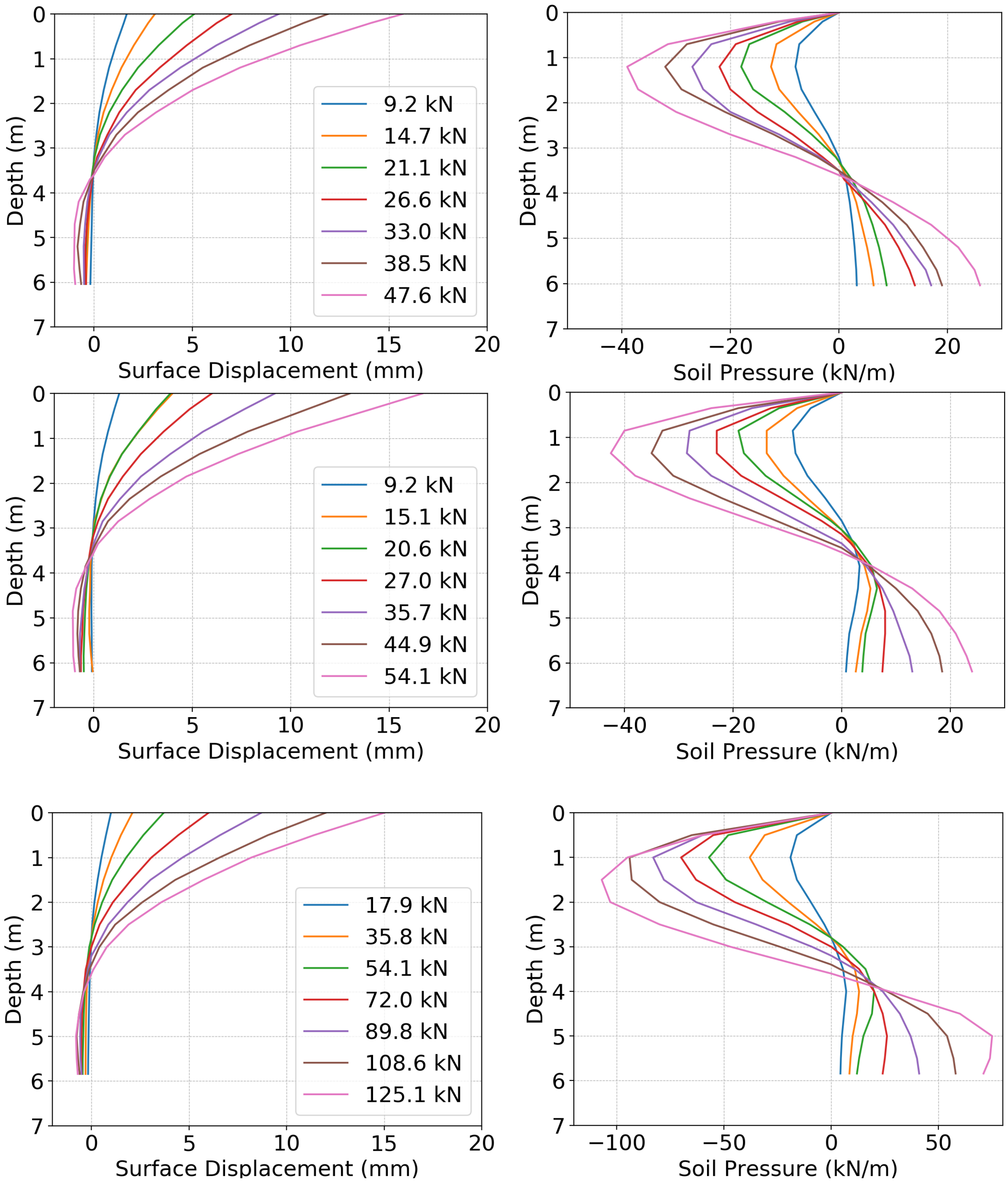

Figure 6-3: 'Probfit' corrected curve fits for cases 2-4 (top to bottom)

equivalent. They appear to respond to loading quite similarly, suggesting that performance is not hugely influenced by installation, unlike for the axial case. The main difference is the level of surging applied during installation, significantly higher for the latter. Case 3's pile is stiffer than case 2's, though most of the discrepancy arises at low displacement - from 10 mm onwards, their respective deformations follow very similar gradients. For case 2 this is slightly lower, though its eccentricity is about 10% higher which would cause fractionally

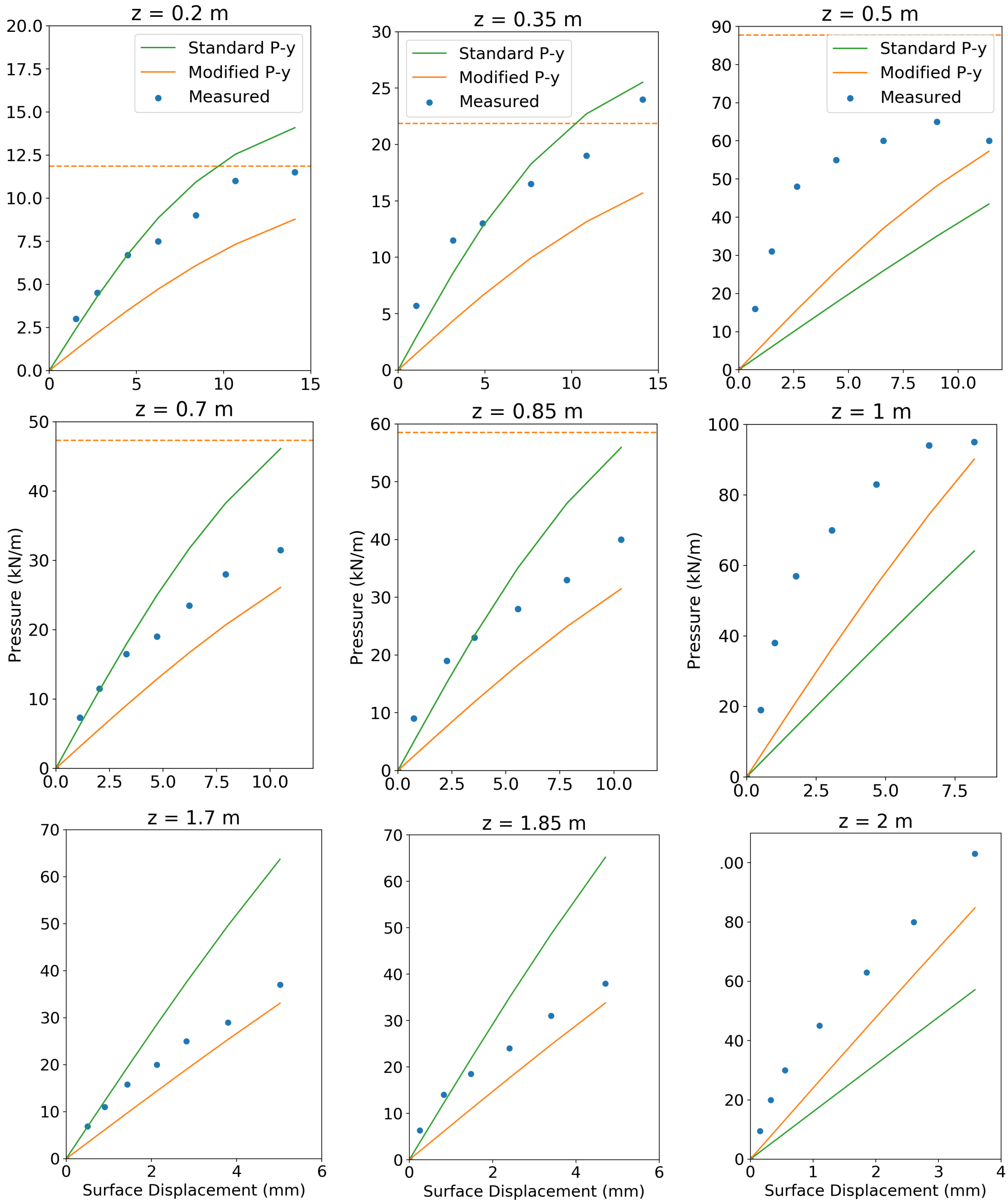

Figure 6-4: P-y curves for cases 2-4 (left to right)

larger head displacement. The difference in eccentricity however is not considered great enough to cause the relatively larger initial difference.

In light of the above, it is hypothesised that the densification of the sand close to the pile during installation (section 2.2) causes the increase in stiffness at small displacements. At small displacements, only soil close to the pile is mobilised, so this increase is significant. As the pile deforms further, the zone of influence grows beyond this region, and the increases in load are determined by the mobilisation of external undisturbed soil. This explains why there is a high initial stiffness for all cases that suddenly drops, why this region is stiffer in case 3 than 2, and why both undergo the same increases in load at larger displacements.

Additionally, the measured P-y curves (while they are known to be imperfect approximations to the true response as explained) support this theory. Notice for example, especially at the greater depths where the ultimate load is not approached (meaning the stiffness should be approximately linear), that the first few data points tend to follow one gradient before a sudden drop to a lesser gradient.

6.2.2 Comparison with Literature

Figure 6-4 makes it clear that the existing P-y approach overestimates the soil pressures experienced by the sheet piles. As explained in section 2.7, the approach is derived from large amounts of empirical data; however, all of the data was obtained using tubular piles, as they are primarily what P-y analysis has been used for. To extend the method to cover sheet piles, it must be modified.

The sheet pile deformation mechanism for lateral movement will be similar to that of a flat plate, due to its sudden edges, and will not be the same as for a circular section. As such, the subgrade reaction modulus and ultimate pressure expressions will be different. They will be adjusted via two terms F_k and F_p, scaling the P-y curve in the displacement and pressure directions respectively. The modified curves of figure 6-4 have had k_{py} and P_u multiplied by $F_k = 0.5$ and $F_p = 0.75$.

With these factors applied, the modified curves now seem to underestimate the true pressures. However, it is argued that this underestimation is equivalent to describing the behaviour excluding the influence of installation (i.e. the factors account for geometry differences only and not installation effects). The installation being beneficial, as explained previously, means this method is conservative. The logic is as follows. Looking at the deeper data points in figure 31, they are within the approximately linear region of the P-y curve, but with an additional ‘hump’, theorised as the result of densification due to surging. The undisturbed stiffness is therefore considered to be the lesser gradient after the initial hump, and $F_k = 0.5$ matches the curves to these regions well. $F_p = 0.75$ matches the ultimate pressure to what it seems to approach for the shallowest data points. Case 2 exceeds this pressure at the highest load, but this point looks to be an outlier anyway, and the limit does not seem unreasonable based on the trend.

Additionally, the python simulation (section 3.4.2) has been run for the parameters of cases 2 and 3 using these factors. Plots of the simulated force-displacement (at surface) curves are compared to those extracted from 'Probfit' in figure 6-5, and further justify the chosen values. Similarly to how the head forces for cases 2 and 3 increased together at larger displacements, this model agrees with the test data beyond the initial hump. In other words, it serves as a base response, and the real response of a pile will have a higher initial stiffness, but then follow its gradient. Since the installation process seems to affect the behaviour far less significantly than for axial behaviour, the undisturbed performance derived from this method is not a bad approximation to the true behaviour. It is also conservative (highly at small displacements but more modestly as it approaches the deflection limits) meaning it is appropriate for design.

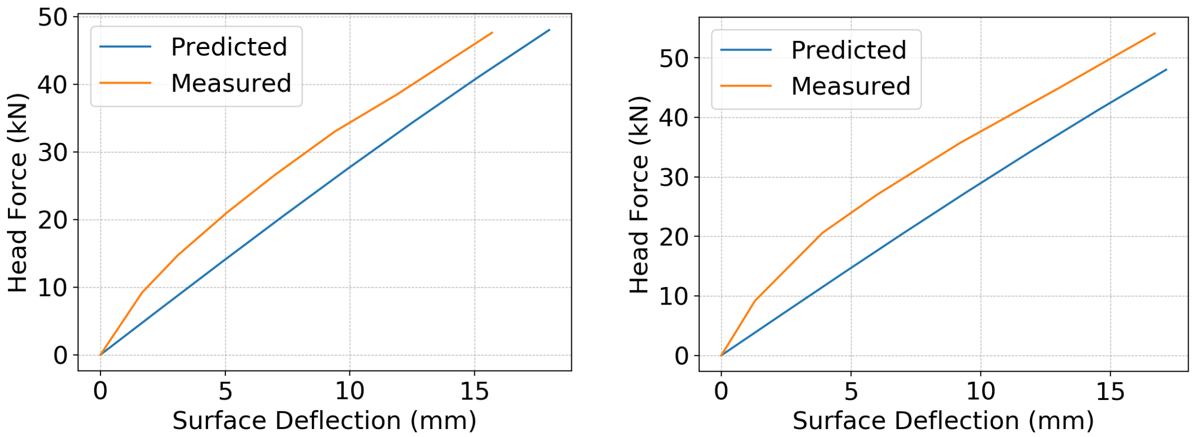

Figure 6-5: Simulated and measured force-displacement response for cases 2 (left) and 3 (right)

Further support for this method comes from looking at the pressures and bending moments produced by the simulations. Table 6-1 shows strong agreement of maximum bending moments and soil pressures along the pile between the simulation and measured results.

Table 6-1: Comparison of simulated and measured maximum moments and pressures

Case	Max. predicted M (kNm)	Max. measured M (kNm)	Max. predicted P (kN/m)	Max. measured P (kN/m)
2	111	106-115	39.5	37-40
3	120	112-120	43.4	41.7-44.8

6.3 Analysis - Grouped Piles

The overall response follows a similar pattern, having secant stiffnesses of between two and three times that seen in cases 2 and 3. Again, there is a high initial stiffness followed by an approximately linear region. This is expected as assuming both behave similarly to a flat plate, the group and individual piles should respond similarly; the only difference is in their widths. In this way, a group of sheet piles is simply equivalent to a larger sheet pile. Determining the group behaviour of sheet piles is therefore analogous to determining how the response varies with width i.e. how the quantities F_k and F_p change.

Firstly, how the current method deals with pile size should be considered. The soil response is solely characterised by two parameters P_u and k_{py}. The function for determining P_u has an inherent linear dependency on D, suggesting that the ultimate horizontal stress is the same regardless of the size of the pile. This may be a reasonable assumption for a circular cross section, as the failure mechanism is likely to be the same. For a sheet pile or wall, however, the mechanism will be different for an individual pile and a long planar wall due to end effects, with P_u/W being lower for the longer case. How sensitive P_u/W is with respect to width is more difficult to know. k_{py} on the other hand is a single constant, independent of the size. This has been disputed for tubular piles (Sorensen and Augustesen, 2016), and figure 6-4 shows shows how unrealistic this is for sheet piles as the stiffness of the group case is much higher than the individual piles. For a flat plate, it would be expected that a plate of double width would receive approximately double the soil resistance at small strains (slightly less due to relatively reduced end effects).

At first, consider that both P_u and k_{py} are linearly dependent on width. That is $F_p = 0.75$ (constant) and $F_k = 0.5 \times W/0.9 = W/(1.8\text{ m})$. Again, the modified curves can be seen in figure 6-4. The comparisons between the predicted and actual P-y data are similar to the individual cases, underestimating the initial stiffness, though the initial hump seems to be much larger here. The ultimate load is now seen to be overestimated by the linear assumption - this is due to being closer to the planar case as explained above.

The primary concern is whether this approach is suitable for design. The P-y simulation, plotted in figure 6-6, shows that the predicted general stiffness is slightly greater than what was measured past the initial region, unlike for the individual cases where the two matched well. Again, this is expected; the soil response degrades as the planar geometry is approached. However, the difference is modest and the result remains conservative due to the initial installation induced hump. While this may not be the case when the soil is less disturbed during installation, it is a reasonable approximation for small pile groups within the range of deflection seen.

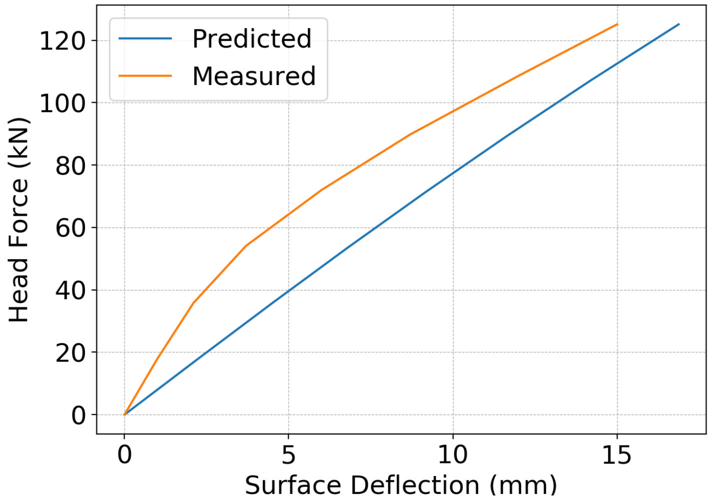

Figure 6-6: Force-displacement response for case 4

The recommended design approach would depend on the level of accuracy and efficiency required. The most crude approach (applicable for small widths) would simply factor the P-y curves by $F_k = W/1.8\text{ m}$ and $F_p = 0.75$, ignore the effects of installation, and run a P-y simulation. A more accurate model would detail more complex functions for F_k and F_p which decrease from the above as W increases. The most accurate model would require a new shape of P-y characteristic, including a third term to account for the installation-induced high initial stiffness. It goes without saying that this would require large amounts of empirical data, and the complexity of the analysis would perhaps outweigh the small gains in performance.

6.4 Design Method

The simulated force-displacement curves (figures 6-5 and 6-6) being approximately linear suggests that the behaviour of the pile within the region of interest (below deflection limits) can be approximated by a single value for overall stiffness, if installation effects are neglected. A simple, conservative design method would therefore derive this stiffness ($K_i = H/y_s$) for a given pile - example design charts are developed in this section.

The force displacement behaviour can be reduced to linear by simply ignoring reductions in soil stiffness with displacement. In other words the hyperbolic P-y curves can be replaced with $P = F_k k_{py} y$. Figure 6-7 shows the force-displacement curves from this linear P-y simulation run for the geometry of case 2, compared to the original simulation. It shows that this formulation indeed outputs a constant stiffness equal to K_i, and that this is a fairly accurate representation of the true behaviour. It is ever so slightly unconservative, but this is more than made up for by the beneficial installation effects.

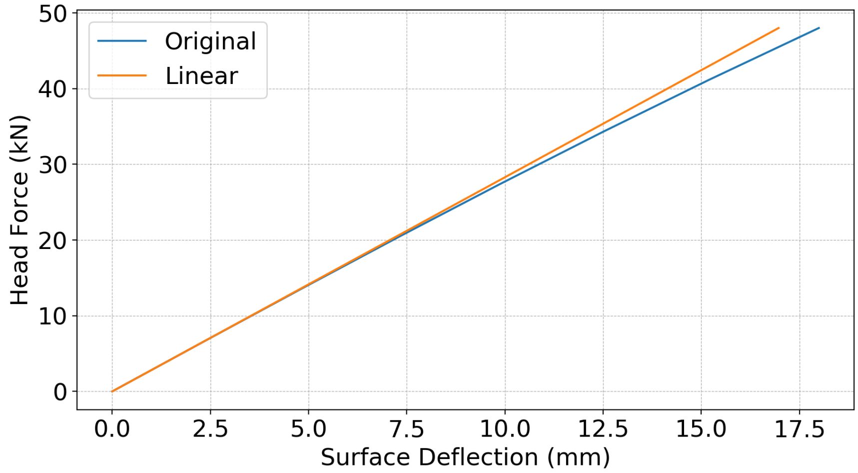

Figure 6-7: Hyperbolic and linear simulations

K_i can be expressed as a function of the following variables:

$$K_i = \frac{H}{y_s} = f\left(L, e_F, EI, k_{py}, W\right) \tag{6.1}$$

Or in dimensionless form:

$$\frac{K_i L^3}{EI} = \bar{K} = f\left(\frac{e_F}{L}, \frac{F_k k_{py} L^5}{EI}\right) = f\left(\frac{e_F}{L}, R_s\right) \tag{6.2}$$

since F_k is a dimensionless function of W. It does not appear as a term on its own as it is by definition coupled to k_{py}. R_s represents the ratio of soil to pile stiffness and influences the deformed shape of a pile. If it is high the pile is long/flexible, and if it is low the pile is short/stiff. The dimensionless surface stiffness can then be plotted over a range of R_s for a variety of e/L, and has been done in figure 6-10 top. There are 5 values of e/L, and two different pile geometries for $e/L = 0.1$. The fact that the lines with different geometries but the same e/L match justifies the validity of this method. In summary, for a given pile, K_i can simply be read off the chart.

The other aspect of pile design is designing for the maximum bending moment, to ensure it is within the capacity of the section. Similarly to figures 6-6 and 6-7, maximum moment-displacement graphs can be extracted (example in figure 6-9) from the P-y simulation. Again, the behaviour is approximately linear within the region of interest. The exact same analysis can therefore be applied, as the maximum moment will be dependent on the same quantities as the head force. This time using a new quantity $m_i = M_{max}/y_s$, the variation of $\bar{m} = m_i L^2/EI$ can be plotted (figure 6-10 bottom).

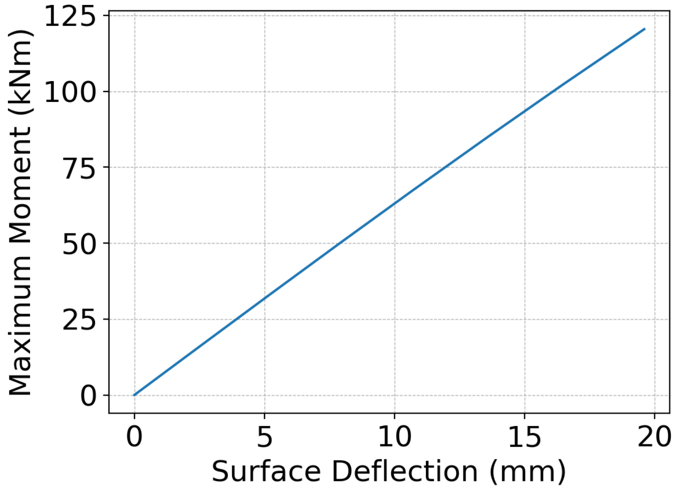

Figure 6-9: Simulated maximum bending moments for case 3

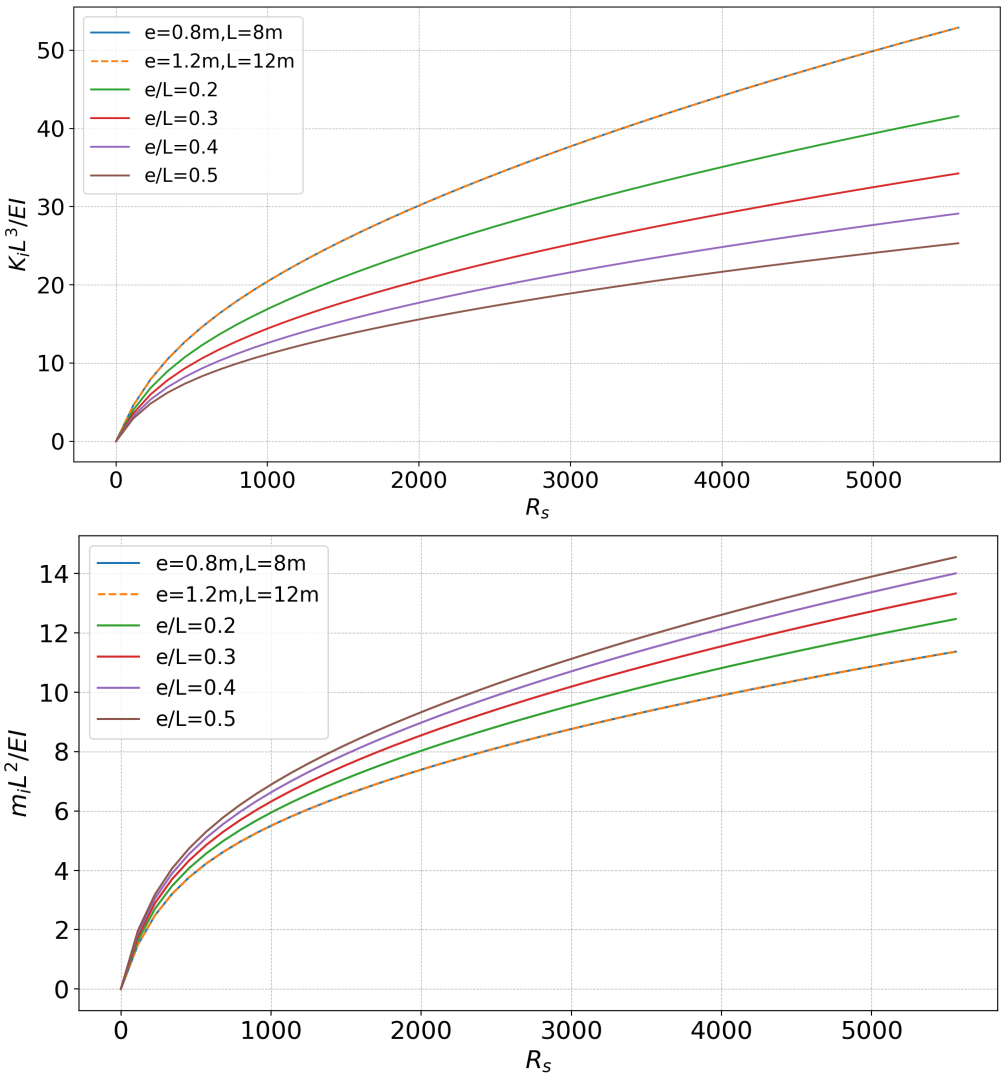

Figure 6-10: Dimensionless design charts

7 Conclusions

7.1 Key Insights

Through full scale pile testing, valuable data has been obtained and analysed, resulting in a number of key insights into the axial and lateral behaviour of sheet piles.

Axial

1. The level of surging during installation is heavily influential towards a sheet pile's vertical capacity, with more cycles leading to greater reduction in capacity. The load observed during installation has been seen to be inherently coupled to the vertical performance, to such an extent that that installation data can even serve as a pile test indicating the pile's capacity (the cycle intersection of the last cycle informs the yield point/design strength).
2. Despite not having a closed section, gross area effects such as vertical arching and plugging are still very prevalent for sheet piles, and central to their behaviour. Both plugged and unplugged modes can be modelled to predict undisturbed capacity; the results can then be scaled to account for installation effects.
3. Plugged: Existing bearing capacity theory may be used to evaluate base resistance. Pile capacity may then be derived as:

$$V_{max,plugged} = \frac{l_p}{l_p - l_s} \cdot A_g(q_{bf} - \gamma' L)$$

4. Unplugged: The horizontal stress acting at the pile wall may be evaluated as bounded by:

$$\sigma_h' = \min\left[\frac{\gamma' A_g}{(l_p - \chi_{mob} l_s)\tan\phi'}\left(e^{\frac{(l_p - \chi_{mob} l_s)K\tan\phi'}{A_g}z} - 1\right), K_p^2\sigma_{v0}'\right]$$

where $0 \leq \chi_{mob} \leq 1$. $\tau_p = l_p\sigma_h' \tan\phi'$ can then be integrated along the length to give capacity.

Lateral

5. For conditions similar to those during testing, within deflection limits the behaviour is approximately linear.
6. The lateral response is only modestly affected by installation conditions, and this effect appears to be a beneficial increase in initial stiffness, so can conservatively be ignored.
7. The P-y method can be applied, but with different parameters to account for non circular geometry. Multiplying k_{py} and p_u by $F_k = W/(1.8\text{ m})$ and $F_p = 0.75$ is a reasonable approach for isolated piles/small pile groups.

8. Dimensionless design charts can be used to give the initial head load and maximum moment per unit surface displacement for a given pile.

7.2 Design Implications

Insight 2 shows that there is a clear trade-off between ease of installation and axial capacity. While this can be seen as a downside, it gives a designer a level of control over the vertical capacity. It is therefore suggested that a pile is designed to meet its lateral performance criteria first. Once an appropriate pile and length has been chosen, its vertical capacity can estimated and compared to axial load requirements. If too low, of course a redesign is necessary, but if it is stronger than required, the designer is able to specify the installation such that the capacity is reduced as much as possible. This will result in the easiest installation possible. As a result of insight 7, the horizontal performance will not be compromised regardless of the chosen level of surging.

To demonstrate the key principles of this project, consider the following example. A sheet pile is to be designed against loads of $V = 300$ kN and $H = 100$ kN at an eccentricity of 0.6 m, with ground conditions similar to that of the testing facility with high water table. Additionally, lateral deflection must not exceed 30 mm. First consider the horizontal case. A process of trial and error in choosing sheet pile and length is necessary. After some attempts, assume the same sheet pile as used in testing and a length of 6 m is chosen.

$$R_s = \frac{F_k k_{py} L^5}{EI} = \frac{(0.9/1.8) \times 8 \times 6^5}{210000 \times 2.2 \times 10^{-4}} = 673 \ , \frac{e_F}{L} = 0.1 \quad \rightarrow \quad \bar{K} = 16.2 \text{ (from figure 6-9)}$$

$$\rightarrow \quad \bar{m} = 4.57$$

$$K_i = 16.2 \times \frac{210000 \times 2.2 \times 10^{-4}}{6^3} = 3.465 \text{ MN/m} = 3.465 \text{ kN/mm}$$

$$m_i = 4.57 \times \frac{210000 \times 2.2 \times 10^{-4}}{6^2} = 5.86 \text{ MN/m}$$

$$K_i > 100/30 = 3.33 \text{ kN/mm} \ \rightarrow \ \text{Deflection sufficient}$$

$$m_i < Z_e \sigma_y / y = (2.2 \times 10^{-4}/0.15) \times 295/0.03 = 14.4 \text{ MN/m} \ \rightarrow \ \text{Section sufficient}$$

Now that a pile has been chosen, its undisturbed vertical capacity can be found. From figure 5-14, this is 1301 kN, meaning a yield of 1301/1.65 = 788 kN. Note while this graph is specifically for this pile type and ground make-up, it is easily automated to take appropriate inputs. $F_{surge} = 0.4$ is therefore appropriate for maximising ease of installation while maintaining sufficient capacity. Figure 5-15 suggests a regime of 40 cycles, meaning a net penetration of 150 mm each cycle. Finally the surging regime can be specified, for example, as 300/150 mm.

7.4 Limitations and Future Work

Throughout this work, there are numerous occasions where data has been insufficient to assert confident relationships. Most severely, in investigating the effects of installation on vertical capacity, there are only two surging regimes which can be directly compared. Where more objective findings have been presented there is still relatively little data, meaning they cannot be evaluated more rigorously, and missing pieces lead to assumptions. For example, when looking at axial penetration, without strain gauges along the length we are only able to compare the total load, and not the distribution, which is heavily significant when considering vertical arching. Finally, all cases harboured very similar conditions; the pile lengths were approximately equal, the same pile shape was used, and the sand was the same, meaning the data cannot be extrapolated to differing conditions confidently.

In order to progress further, future work best be targeted at the following areas:

- Similar experiments with different pile shapes, sizes and lengths.
- Similar experiments in alternative types of sandy soil, such as those with different ϕ' or carbonate soils.
- Retrieving earth pressure data close to the wall of the central soil column, in the normal direction to the external soil boundary, at multiple depth points.
- Retrieving strain data to analyse axial force distribution.
- Using a greater variety of installation methods, obtaining as much data as possible.
- Lateral performance of much longer walls, as well as numerical modelling of lateral deformation mechanisms of sheet piles to better inform F_k and F_p.

This work has provided logical explanations for what is observed based on available data, and provides direction for their potential implications for design. The proposed models and methods all follow the measured trends and make sense in accordance with existing knowledge at a high level, but lack of data means that the details cannot be scrutinised and should be taken with caution. With further evidence, the ideas presented in this report may or may not be supported, but they seem to make sense of what is available.

References

API (2000). Recommended Practice for Planning, Designing and Constructing Fixed Offshore Platforms—Working Stress Design.

Baldi, G., Bellotti, R., Ghiona, V., Jamiolkowski, M., Pasqualini E. (1986). Interpretation of CPTs and CPTUs. Part II: drained penetration of sands. 4th Int. Geotechnical Seminar on Field Instrumentation and in-situ Measurements, NTI, Singapore (1986), p143-156.

Bolton, M.D. (1986). The strength and dilatancy of sands. Géotechnique, vol. 36 (1), p65-78.

BSI (2004). Eurocode 7: Geotechnical design - Part 1: General rules.

Burali d'Arrezo, F. (2015). Installation effects due to pile surging in sand. University of Cambridge Department of Engineering.

Jamiolkowski, M., Lo Presti, D. C. F., Manassero, M. (2001). Evaluation of Relative Density and Shear Strength of Sands from CPT and DMT. Symposium on Soil Behavior and Soft Ground Construction Honoring Charles C. "Chuck" Ladd, p201-238.

JGS (2010). JGS 1810-2010: Method for Lateral Load Test of Piles.

JGS (2002). JGS 1811-2002: Method for Static Axial Compressive Load Test of Single Piles.

Kishida, H., Isemoto, N. (1977). Behaviour of sand plugs in open end steel pipe piles. Proc. 9th Int. Conf. Soil Mechanics and Foundation Engineering, Tokyo, p601-604.

O'Neill, M. W., Murchison, J. M. (1983). An Evaluation of P-y Relationships in Sands. University of Houston Department of Civil Engineering.

Prandtl, L. (1920). Uber die Harte plastischer Korper.

Prasad, Y. V. S. N., Chari, T.R., (1999). Lateral capacity of model rigid piles in cohesionless soils. Soils and Foundations, vol. 39 (2), p21-29.

Randolph, M. F., Leong, E.C., Houlsby, G. T. (1991). One dimensional analysis of soil plugs in pipe piles. Géotechnique, vol. 41 (4), p578-598.

Rankine, W. (1856). On the stability of loose earth. Philosophical Transactions of the Royal Society of London, Vol. 147, p9-27.

Reese, L.C., Matlock, H. (1956). Non-dimensional solutions for laterally-loaded piles with soil modulus assumed proportional to depth. Proc. 8th Texas Conference on Soil Mechanics and Foundation Engineering, Austin, Texas, p1-41.

Reese, L.C., W.R. Cox, Koop, F.D. (1974). Field testing and analysis of laterally loaded piles in sand. Proc. 6th Annual Offshore Technology Conference, Houston, Texas, vol. 2, 473-485.

Reese, L. C., Van Impe, W. F. (2010). Single Piles and Pile Groups Under Lateral Loading.

Schmertmann, J.H., (1976). An Updated Correlation Between Relative Density, Dr, and Fugro-Type Electric Cone Bearing, qc. Vicksburg, MS, Report DACW 39-76 M6646.

Sørensen, S. P. H., Augustesen, A. H. (2016). Small-displacement soil-structure interaction for horizontally loaded piles in sand. Proc. 17th Nordic Geotechnical Meeting, Reykjavic, p775-786.

Soubra, A.H., Regenass, P. (2000). Three-Dimensional Passive Earth Pressures by Kinematical Approach. Journal of Geotechnical and Geoenvironmental Engineering, vol. 126 (11), p969-978.

Alves, F. S., Lopes, F. R., Danziger, F. A. B., Santana, C. M. (2020). Study of plugging of steel H piles, jacked in sand, in a calibration chamber. International Journal of Physical Modelling in Geotechnics.

White, D. J., Bolton, M.D. (2002). Observing friction fatigue on a jacked pile. Proc. Workshop on Constitutive and Centrifuge Modelling: Two Extremes, p347-354

White, D. J., Lehane B. (2004). Friction fatigue on displacement piles in sand. Géotechnique, vol. 54 (10), p645-658.

Risk Assessment

Over summer, field testing was carried out at a Giken test facility in Japan. Due to the nature of the testing, there were multiple hazards that had to be considered, and various precautions were taken. On arrival, before testing began, a general review of Giken's safety health and safety policy and procedures was provided, detailing routes and site mapping, important locations such as fire assembly points, appropriate PPE to be worn and general advice. Following this, many unique hazards were identified during testing. Every morning, the full team participated in a health and safety meeting, where risks specific to the day's tasks were evaluated and preventative measures detailed. The most common risks were trip hazards due to the multitude of wires from the sensors, dehydration and heatstroke, head collision when working in cramped spaces, and danger of injury from contact with active heavy machinery. Preventative measures involved wearing PPE at all times on site, conscious efforts to ensure water and salt intake was sufficient, maintaining clear work spaces and all other than designated operators staying well clear of active machinery. The rules and guidance were followed throughout and no incidents occurred.

As a result of testing being completed by the time the academic year started, little to no experimental work was expected. The initial risk assessment detailed computer use as the primary activity. Back, neck and eye strain were the main hazards, and were mitigated well by appropriate structuring of work sessions. Standard geotechnical laboratory testing was identified as another potential low-risk activity, though this was not carried out in the end, and thus no further risk was encountered. The initial risk assessment was therefore sufficient despite its brevity.